Analysis of joint formation mechanisms for self-piercing riveting (SPR) process with varying joining parameters

Huan Zhao[a], Li Han[b], Yunpeng Liu[a] and Xianping Liu[a,*]

[a] School of Engineering, University of Warwick, Coventry CV4 7AL, UK

[b] Hansher Consulting Ltd., Coventry, UK

* X.Liu@warwick.ac.uk

Abstract:

By combining experimental SPR tests with a finite element (FE) model, the influences of top sheet thickness (T_t), bottom sheet thickness (T_b) and rivet length (L) on the joint formation mechanisms were systematically investigated in this study. Single factor experiments were firstly conducted to uncover the three joining parameters' effects on the joining results. Interrupted SPR tests were also performed to confirm the prediction accuracy of the FE model on the joint formation process. Then, the joint formation mechanisms were analyzed by numerically inspecting the events during the riveting process, including the sheet deformation behaviors, rivet shank flare behavior and formation of quality indicators. The results revealed that the joining parameters affected the interlock formation by directly altering the positions of two interlock boundaries. The rivet shank flare behavior was apparently affected by the T_t and T_b, but less influenced by the L. The formation of remaining bottom sheet thickness at the joint center (T_c) was significantly affected by the T_t and T_b. Rapid reduction of the T_c occurred before the top sheet was penetrated and after the rivet cavity was fully filled. Meanwhile, it is highlighted that the FE model is an excellent tool to analyze SPR joint formation.

Keywords: SPR joint; Formation mechanisms; FE model; Interrupted experimental test; Sheet thickness; Rivet length.

1 Introduction

During the last few decades, lightweight materials have been increasingly used in the automotive industry to reduce the vehicle weight without compromising its performances [1]. Self-piercing riveting (SPR) technique experiences a rapid development under such circumstances, and has been widely adopted by many automobile companies (e.g., BMW, JLR and Audi) as the major joining approach to assemble the aluminum car body-in-white (BIW) structures [2]. The SPR process is consist of four major steps as shown in **Fig. 1**, including (a) clamping; (b) piercing; (c) flaring and (d) releasing tools. The multiple sheets are tightly connected by a mechanical interlock formed between the rivet shank and the bottom sheet. As a mechanical joining approach, the SPR has many advantages in the connections of thin-walled structures, such as effective for stacks with two or three layers [3], suitable for similar and dissimilar materials, and compatible with various surface conditions

(e.g., coatings or paintings). In recent years, some new joining approaches based on the SPR technique have also been proposed to further improve the joint quality and mechanical performance, such as the friction self-piercing riveting (F-SPR) [4][5], the electromagnetic self-piercing riveting (E-SPR) [6], the electroplastic self-piercing riveting (EP-SPR) [7] and the thermally assisted self-piercing riveting (TA-SPR) [8].

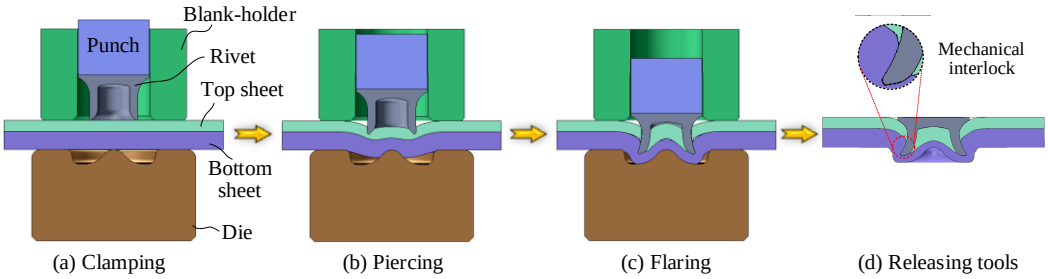

Fig. 1 Schematic of the four steps during the self-piercing riveting process

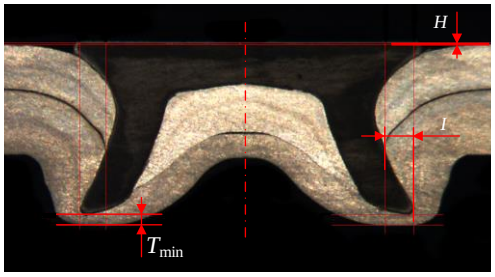

Fig. 2 Schematics of the joint cross-sectional profile and three quality indicators

The SPR joint quality is usually assessed by three quality indicators measured on the joint cross-sectional profile [9,10] as shown in **Fig. 2**: the rivet head height (H), the interlock (I) and the minimum remaining bottom sheet thickness (T_{min}). The H directly affects the cosmetic appearance of the connected structure and the joint corrosion resistance [11]. The I is very important for the joint mechanical strengths and failure behaviors. SPR joints with a too small I usually have low shearing strengths, and more likely undergo failures of the rivet shank pulled out from the bottom sheet [12]. The T_{min} is a critical indicator for the joint corrosion resistance and water-proof performance. Zero or negative T_{min} would lead to moisture or water invasion. This would accelerate the galvanic corrosion between the steel rivet and aluminum sheets, and cause premature corrosion failure of SPR joints [13][14]. Over the last few decades, a great number of experimental studies have been carried out to investigate the effects of different joining parameters on the SPR joint quality, such as the sheet material and thickness [15], the rivet material [16] and geometry [17], the die geometry [12] and the riveting speed [18]. Recent years, many finite element (FE) models of SPR process have also been successfully developed and utilized to facilitate the analysis of joining parameters' effects on the joint quality, such as the die geometric parameters [19,20], the initial sheet temperature [21] and the sheet thickness ratio [22]. Detailed reviews of the experimental and numerical investigations of SPR technique can be found in [9,23,24]. By analyzing the accessible studies relevant to the SPR technique, it was noticed that most of them focused on establishing the relationships between joining parameters and specific joint quality indicators (e.g., I and T_{min}). Conclusions from these existing studies were mainly drawn by simply analyzing the final joint cross-sectional profiles. To the authors' knowledge, little efforts were made to investigate the joint formation mechanisms during the SPR process with different joining parameters, e.g., how the I and T_{min} are formed, how different joining parameters

affect their formations and final magnitudes. For example, previous studies have widely acknowledged that the top sheet thickness (T_t), bottom sheet thickness (T_b) and rivet length (L) are three critical parameters affecting the SPR joint quality [9] [20,23]. Some studies have also reported the influences of these three joining parameters on the magnitudes of joint quality indicators (e.g., I and T_{min}) [15,16,22]. However, none of the existing studies addressed the reasons why the final magnitudes of joint quality indicators changed as the joining parameters altered from the view of joint formation. This is attributed to the inconvenience to experimentally observe the deformation behaviors of rivet and sheets during the SPR process. In-depth understanding of the joint formation mechanisms throughout the SPR process will be a great contribution to the development and practical applications of the SPR technique in terms of new joint design and new types of rivets and dies.

Interrupted experimental SPR test, in which the riveting process is stopped at different positions, offers a way to experimentally analyze the riveting process and explore the formation mechanisms of different SPR joints. For example, with the help of interrupted tests, Haque et al. [25] successfully linked the changes of the load-displacement curve with the events in the SPR process and concluded that the SPR joining process could be monitored with the load-displacement curve. The same authors [26] also identified the flare behavior of rivet shank during the SPR process by interrupted experimental tests, and proposed an empirical linear equation to calculate the rivet shank flare distance. Li [27] experimentally investigated the influences of interface conditions between the two sheets on the deformation behavior of rivet shank during the SPR process. However, the interrupted experimental SPR test is extremely time and money-consuming because a large number of specimens are required for each joint configuration. Due to this limitation, it was rarely employed in the accessible SPR studies and is also unlikely to become a mainstream research approach for the SPR technique. Recent years, the FE model of SPR process has become increasingly powerful and accurate. It is also an effective tool for the inspection of joint formation process and for the collection of useful information inside the joining region. Compared with the interrupted experimental SPR test, it requires far less investment in time and money. Meanwhile, instead of only several joint cross-sectional profiles at the interrupted positions, the whole joint formation process can be conveniently observed with the FE model [28–30]. Therefore, the FE model is an excellent alternative to the interrupted experimental SPR test for investigating the joint formation mechanisms.

In this study, the formation mechanisms of SPR joints with varying T_t, T_b and L were systematically investigated by combining the laboratory experimental SPR test with a verified FE model. Single factor experiments were firstly conducted to investigate the impact of three joining parameters on the deformed shapes of rivet and sheets, and to uncover the variation trends of different joint quality indicators. Before using the FE model to assist the analysis of joint formation mechanisms, its effectiveness for SPR joints from the single factor experiments was confirmed by comparing the simulated and experimentally tested joint cross-sectional profiles, joint quality indicators and load-displacement curves. Interrupted experimental SPR tests were also performed to confirm the prediction accuracy of the FE model on the deformation behaviors of rivet and sheets, and on the formations of joint quality indicators during the SPR process. Then, the impact of the three joining parameters (i.e., T_t, T_b and L) on the SPR joint formation was experimentally and numerically analyzed. The results from this research will contributed to in-depth understanding of the joint formation mechanisms, and be beneficial for the design

of new SPR joints with varying sheet thicknesses.

2 Experiment procedure

2.1 Single factor experimental tests

As listed in **Table 1**, single factor experiments were carried out to investigate the impact of the top sheet thickness (T_t), bottom sheet thickness (T_b) and rivet length (L) on the formation of SPR joints, especially the formation mechanisms of the interlock (I) and the remaining bottom sheet thickness. The sheet material used throughout the study is aluminum alloy AA5754, and the semi-tubular rivets are made of boron steel with the hardness 280±30HV10. **Table 2** shows the basic mechanical properties of the rivet and sheet materials. A pip die (Type-A) was adopted in the single factor experiments. **Fig. 3** shows the nominal dimensions of the semi-tubular rivet and the pip die (Type-A). Four top sheet thickness levels (i.e., 1.0 mm, 1.2 mm, 1.5 mm and 2.0 mm) were used in the joints J1-1~J1-4. Four bottom sheet thickness levels (i.e., 1.0 mm, 1.5 mm, 1.8 mm and 2.0 mm) were utilized in the joints J2-1~J2-4. Three rivet length levels (i.e., 5.0 mm, 6.0 mm and 6.5 mm) were used in the joints J3-1~J3-3. The specimen size is 40 mm×40 mm as shown in **Fig. 4**. Other joint conditions were kept the same throughout the experiment. All the SPR joints were made using a servo SPR system manufactured by Tucker GmbH shown in **Fig. 5**. The riveting speed is set to 300 mm/s, and the clamping force on the blank-holder is approx. 5.0kN~6.0kN controlled by a compressed spring. For easier comparison and consistence, the rivet head height (H) in all SPR joints was controlled to the same value (i.e., −0.10 mm) by predefining the rivet displacement in the SPR system. To ensure the effectiveness of the experiment results, three repeats for each joint configuration were conducted.

All the specimens were sectioned through the joint central plane, and then lightly polished to capture the joint cross-sectional profiles. As shown in **Fig. 6**, the rivet head height (H) and the interlock (I) for each joint were measured from the joint cross-sectional profiles. The joint quality indicator T_{min} can appear at any part of the deformed bottom sheet (green dashed line in **Fig. 6**), and its position varies from joint to joint. To quantitively evaluate the joining parameters' impact on the formation of remaining bottom sheet thickness, the remaining bottom sheet thickness at the joint center (T_c) and under the rivet tip (T_{tip}) for each joint were measured. In addition, the load-displacement curve of each joint during the riveting process was also recorded.

Table 1 Design of the single factor experiments

Joint no.	Thickness (mm)		Rivet (Boron steel)	Die
	Top sheet/T_t (AA5754)	Bottom sheet/T_b (AA5754)		
J1-1	1.0	1.8	C5.3*5.0	Pip die (Type-A)
J1-2	1.2	1.8	C5.3*5.0	
J1-3	1.5	1.8	C5.3*5.0	
J1-4	2.0	1.8	C5.3*5.0	
J2-1	1.2	1.0	C5.3*5.0	
J2-2	1.2	1.5	C5.3*5.0	
J2-3	1.2	1.8	C5.3*5.0	
J2-4	1.2	2.0	C5.3*5.0	
J3-1	1.2	1.8	C5.3*5.0	
J3-2	1.2	1.8	C5.3*6.0	

J3-3	1.2	1.8	C5.3*6.5

Table 2 Mechanical properties of the rivet [31] and sheet materials [32]

Material	Young's Modules (GPa)	Poisson's ratio	Elongation (%)	Thermal expansion coefficient (1/°C)
AA5754	70	0.33	22	2.4E-5
Boron steel	200	0.30	--	1.2E-5

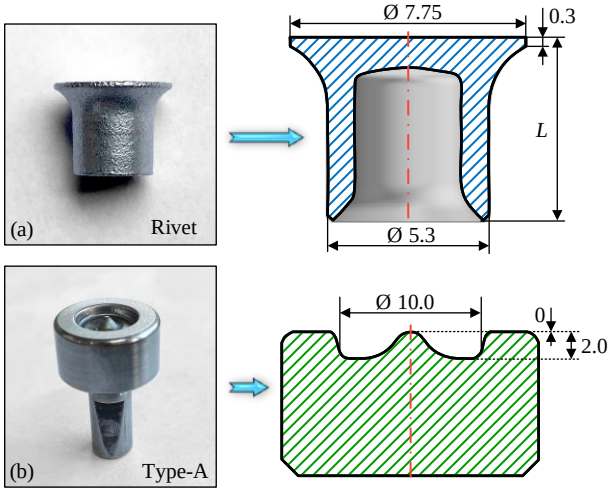

Fig. 3 Dimensions of (a) the semi-tubular rivet and (b) the pip die (Type-A) (in mm)

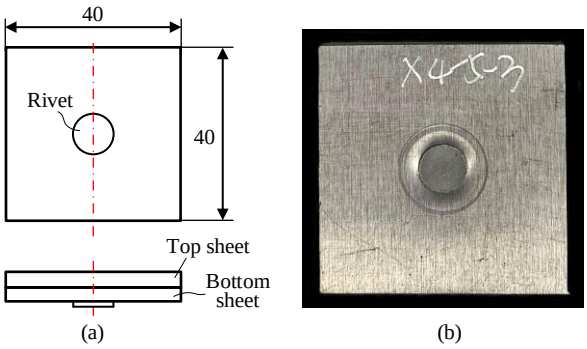

Fig. 4 Specimens dimensions of the SPR joints (in mm)

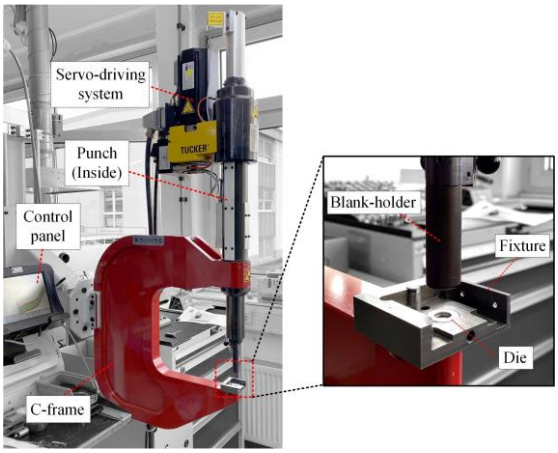

Fig. 5 Structure of the servo SPR system manufactured by Tucker GmbH

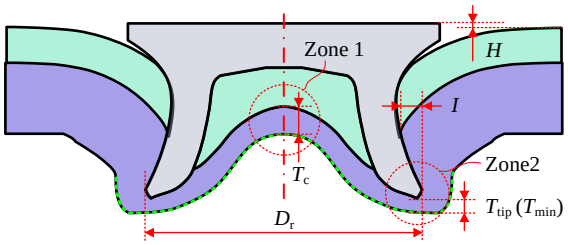

Fig. 6 Characteristics measured on the joint cross-sectional profile for the analysis of SPR joint formation

2.2 Interrupted experimental tests

Interrupted experimental tests were also conducted to confirm the effectiveness of a previously developed FE model (described in the following section) on the prediction of SPR joint formation, including the deformation behaviors of sheets, the flare behavior of rivet shank and the formation process of joint quality indicators. The interrupted experimental test means that a continuous SPR process is manually stopped at several pre-defined positions. It is the only experimental approach to directly observe the joint formation at different riveting stages [33]. As listed in **Table 3**, the riveting process of the selected SPR joint (1.2 mm+2.0 mm AA5754 sheets and 6.0 mm long boron steel rivet) was interrupted at five positions by controlling the magnitude of rivet head height (H) (i.e., 4.0 mm, 3.0 mm, 2.0 mm, 1.0 mm and 0.0 mm). **Fig. 7** shows the dimensions of the pip die (Type-B) used in the interrupted experimental tests. Other experimental conditions were kept the same as that used in the above single factor experiments. All the specimens were sectioned through the joint central plane, and then lightly polished to capture the joint cross-sectional profiles at different riveting stages. Meanwhile, the interlock (I), the T_c and the deformed rivet shank diameter (D_r) (see **Fig. 6**) at each stopped position was also measured.

Table 3 Design of the interrupted experimental tests

Joint no.	Thickness (mm)		Rivet head height/H (mm)	Rivet (Boron steel)	Die
	Top sheet/T_t (AA5754)	Bottom sheet/T_b (AA5754)			
J4-1	1.2	2.0	4.0	C5.3*6.0 (280±30HV10)	Pip die (Type-B)
J4-2			3.0		
J4-3			2.0		
J4-4			1.0		
J4-5			0.0		

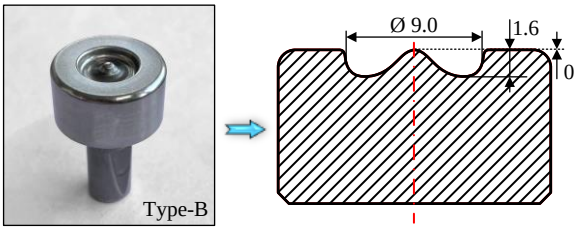

Fig. 7 Dimensions of the pip die (Type-B) used in the interrupted experimental SPR tests (in mm)

3 FE model of the SPR process

3.1 Description of the FE model

The FE model of SPR process previously developed by the authors is shown in **Fig. 8**. It was established with

the software Simufact.Forming, and its prediction accuracy for SPR joints with AA5754 sheets and boron steel rivet has been intensively validated [34]. All the freedoms of die were fixed while the sheet edges can move freely during the riveting process. A 5.3kN clamping force (F_1) was applied on the blank-holder to clamp the top and bottom sheets together. The punch had a constant speed (v_1=300 mm/s) and moved downward to press the rivet into the sheets. The punch, blank-holder and die were modelled as rigid bodies, while the boron steel rivet and AA5754 sheets were modelled as elastic-plastic bodies. As shown in **Fig. 9**, plastic stress-strain curves were implemented to model the material deformations of the rivet and sheets. The temperature effect on the material properties was considered for the AA5754 sheets but not considered for the boron steel rivet. This is because the maximum temperature within the joining region is usually lower than 250 °C [35], and imposes limited influences on the mechanical properties of the boron steel. Uniaxial tensile tests at four different temperatures were carried out to determine the plastic stress-strain curves for the AA5754 sheets [35], whilst only the uniaxial tensile test at room temperature was performed to get the plastic stress-strain curve for the boron steel rivet. All the deformable parts were meshed using the quad element with four gauss points. The mesh sizes for the rivet, the top sheet and the bottom sheet were set to 0.10 mm, 0.10 mm and 0.12 mm respectively. Automatic element re-meshing was applied to deal with the severe element distortion caused by large plastic deformations of the top and bottom sheets. A geometric criterion was employed to model the top sheet fracture and the threshold thickness was set to 0.04 mm. The Coulomb friction model was adopted and the friction coefficients between different contact parts are given in **Table 4**. Due to the difficulties of directly measuring the friction coefficients, the suitable friction coefficient at each interface was determined with the inverse method frequently used in the existing numerical studies [36]. To ensure efficiency, the springback of SPR joints during the tools (i.e., punch, blank-holder and die) releasing process was not simulated. More details about the FE model can be found in [34,37].

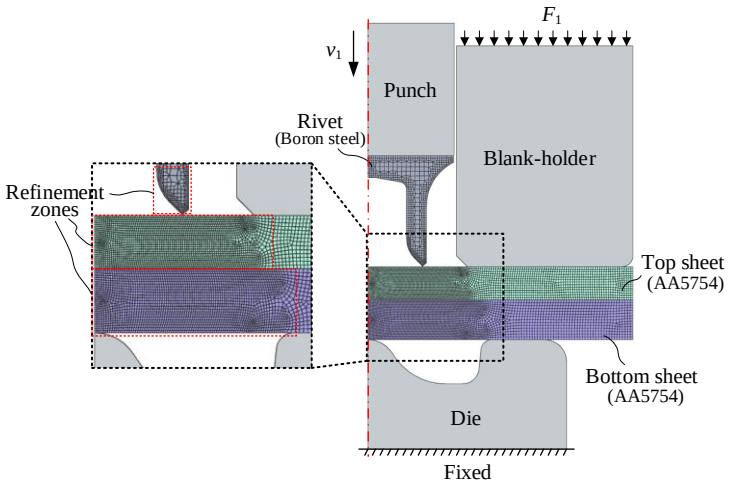

Fig. 8 Schematic of the two-dimensional (2D) axisymmetric FE model of SPR process

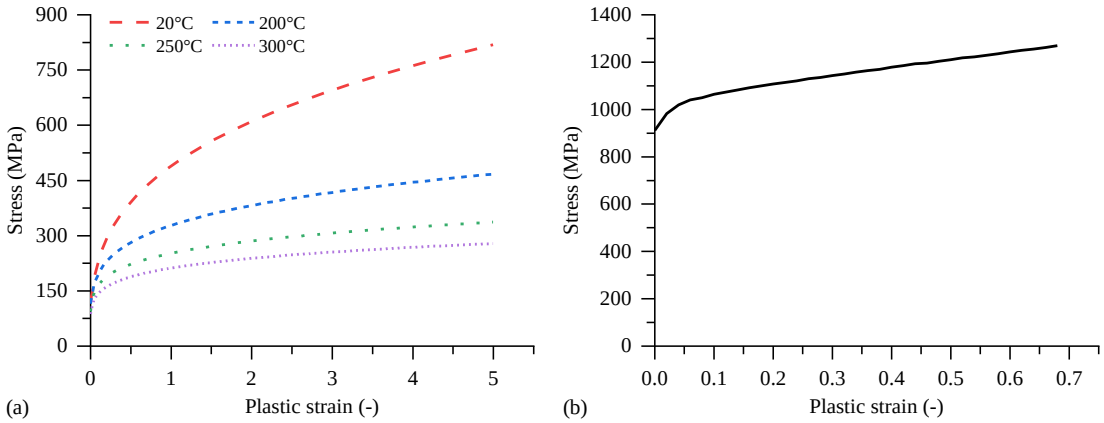

Fig. 9 Plastic stress-strain curves for (a) the aluminium alloy AA5754 (strain rate=1s^{-1}) [35] and (b) the boron steel rivet (20°C, strain rate=0.01s^{-1}) [37]

Table 4 Friction coefficients used in the simulation model [37]

Contact pairs	Punch-Rivet	Blankholder-sheets	Rivet-Sheets	Top sheet-Bottom sheets	Bottom sheet-Die	Others
Friction coefficients	0.10	0.10	0.10	0.10	0.22	0.10

3.2 Effectiveness of the FE model

Before using the FE model to assist the analysis of joint formation mechanisms, its effectiveness for the SPR joints from single factor experiments (**Table 1**) was firstly confirmed. The prediction performance of the FE model on SPR joint formation was also verified by comparing the simulation results with that from the interrupted experimental tests (**Table 3**).

3.2.1 For SPR joints from single factor experiments

Fig. 10 shows the simulated and tested cross-sectional profiles of the joints J1-1~J3-3. It can be seen that the predicted shapes of the rivet and sheets showed good agreements with the experimentally tested ones. The joint defects, such as the gaps formed between the top sheet and the rivet (e.g., Gap 1 in **Fig. 10**(d)), between the top and bottom sheets (e.g. Gap 3 in **Fig. 10**(b)), were accurately identified with the developed FE model (Gap 2 and Gap 4). The severely localized deformation of the top sheet around the rivet shank (e.g., Zone 1 and Zone 3) was also accurately predicted (e.g., Zone 2 and Zone 4). Comparisons between the simulated and tested quality indicators are given in **Fig. 11**. By visual observation, it can be found that the predicted values of the I, T_c and T_{tip} matched well with that from the experimental SPR tests. The calculated mean absolute error (MAE) for the I, T_c and T_{tip} are 0.066 mm, 0.042 mm and 0.115 mm respectively, and the corresponding mean absolute percentage error (MAPE) are 10.5%, 12.9% and 19.7%. Because the changing trend of riveting force (F_r) is closely linked with the events happen during the riveting process [25], the simulated and experimentally measured load-displacement curves of the joints J1-1~J3-3 are also compared as shown in **Fig. 12**. It is obvious that the predicted changing trends and magnitudes of the F_r were almost identical with that from the experimental SPR tests. Based on the above comparisons, it can be concluded that the developed FE model has

a high prediction accuracy for the studied joint configurations.

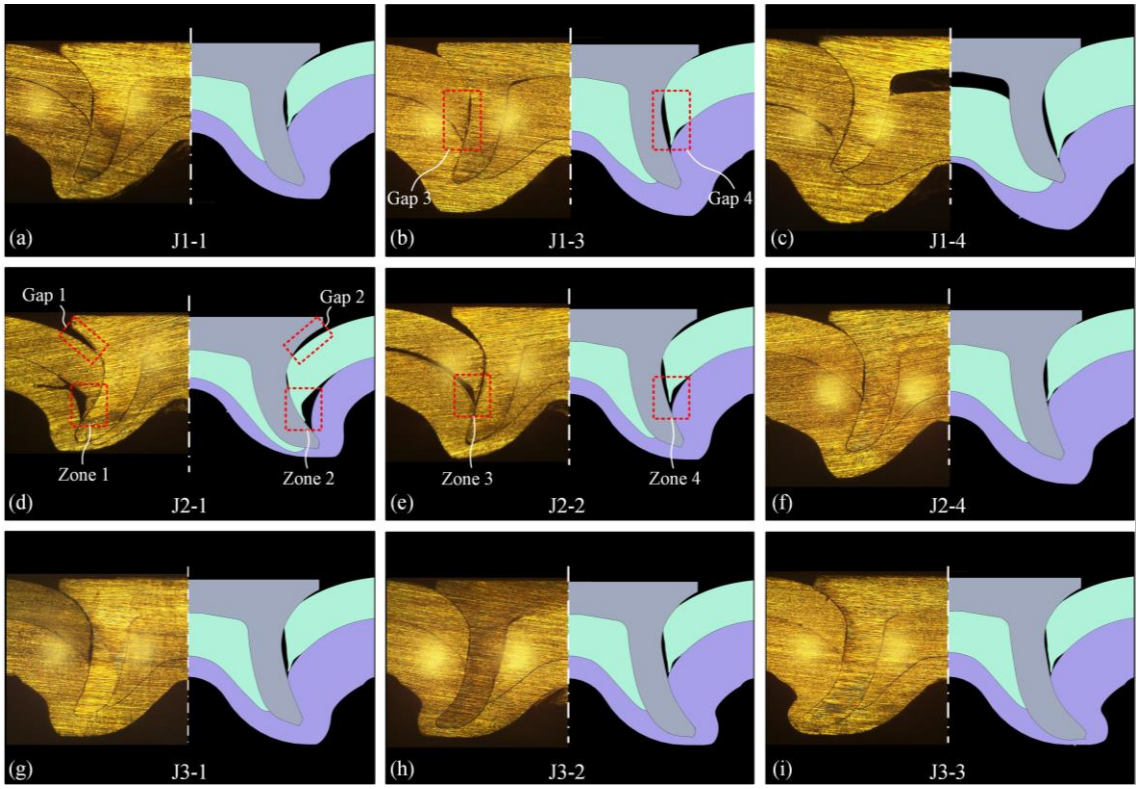

Fig. 10 Comparisons between the experimentally tested and the simulated cross-sectional profiles of the SPR joints J1-1~J3-3

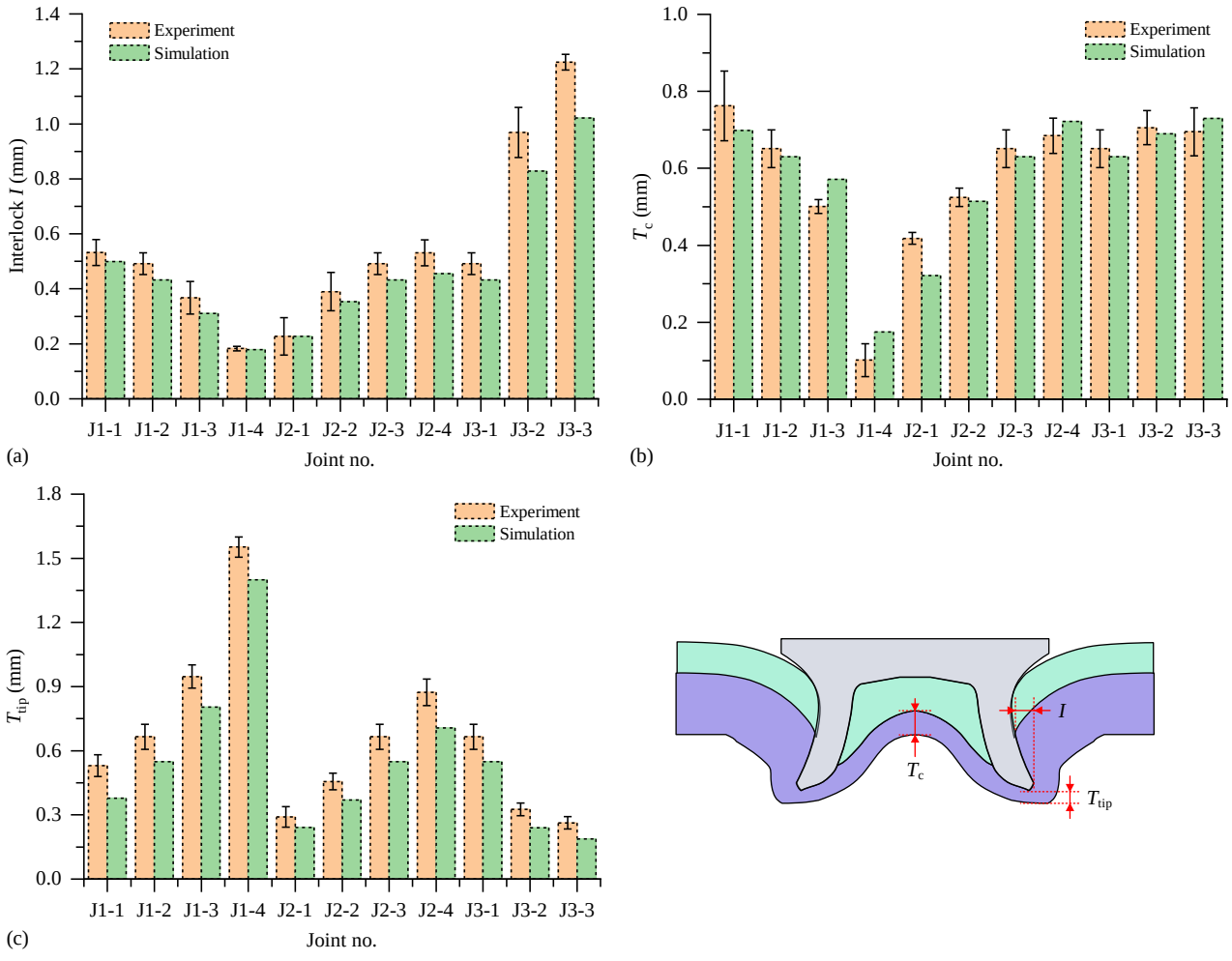

Fig. 11 Comparisons between the simulated and the experimentally tested (a) interlock I, (b) remaining bottom sheet thickness at the joint center T_c and (c) remaining bottom sheet thickness under the rivet tip T_{tip} in the joints J1-1~J3-3

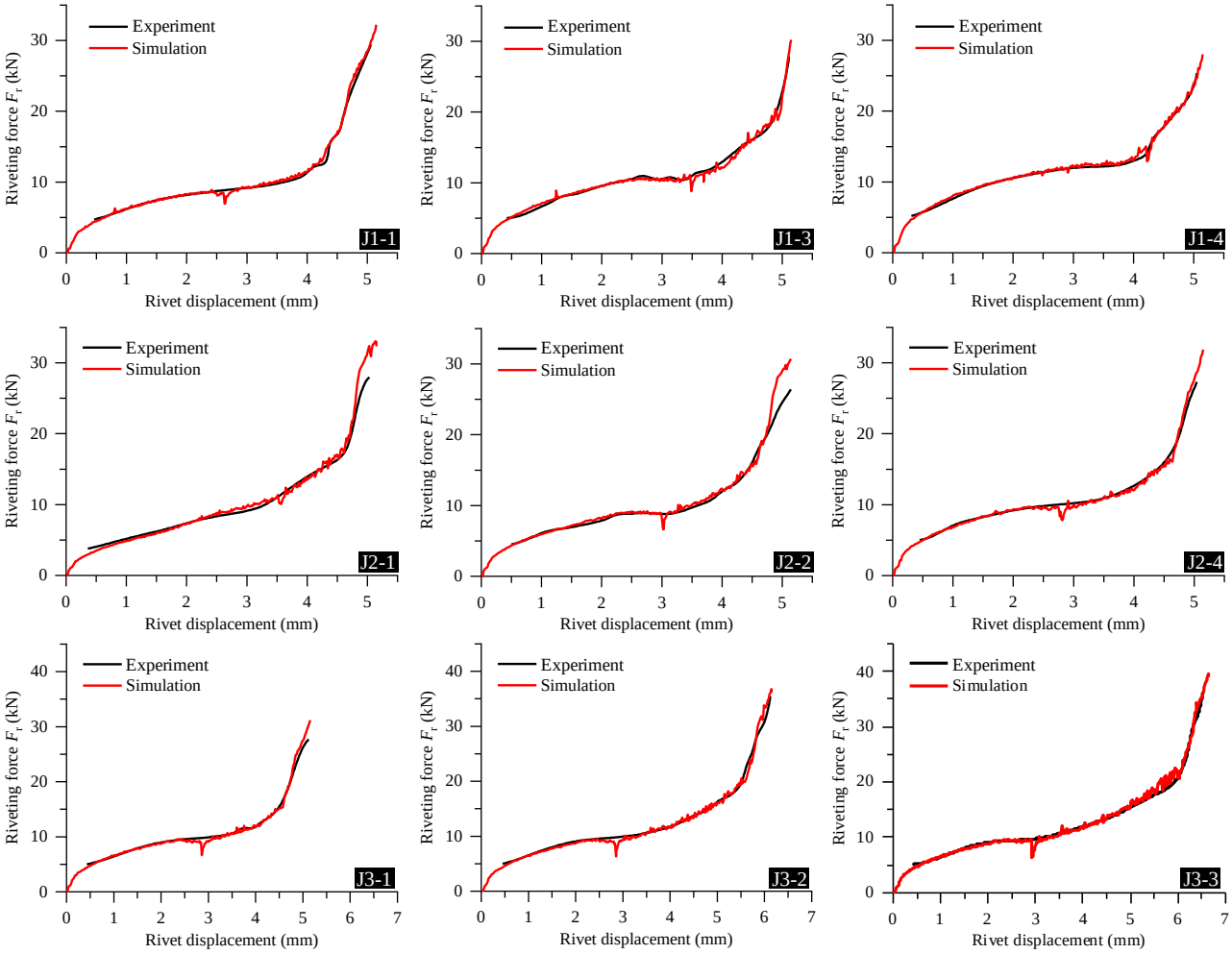

Fig. 12 Comparisons between the simulated and the experimentally tested load-displacement curves of the joints J1-1~J3-3

3.2.2 For the SPR joint formation process

Comparisons between the cross-sectional profiles of the joints J4-1~J4-5 from the FE simulations and interrupted experimental tests are presented in **Fig. 13**. It can be seen that the deformed shapes of the rivet and sheets at each riveting stage from the FE model are matched well with that from the interrupted experimental tests. The gap formed between the two sheets (Zone 1) and the local deformation on the bottom sheet (Zone 3) were also accurately predicted by the FE model (Zones 2 and 4). The simulated and tested variation curves of the deformed rivet shank diameter (D_r), the remaining bottom sheet thickness at the joint center (T_c) and the interlock (I) are compared in **Fig. 14**. It can be seen that both of the simulated and tested D_r first increased slowly and then increased rapidly with the decline of the H as shown in **Fig. 14**(a). Both of the simulated and tested T_c first decreased rapidly and then kept almost constant before the second rapid decline occurred as shown in **Fig. 14**(b). Both of the simulated and tested I started increasing rapidly from around H=3.0 mm and its increasing speed kept almost constant with the decline of the H as shown in **Fig. 14**(c). These results indicated that the changing trends of the D_r, T_c and I were accurately predicted by the FE model (red dash lines in **Fig. 14**). It can be found that the predicted and tested magnitudes of the D_r, T_c and I at varying H also showed reasonable agreements. Therefore, the developed FE model is capable of predicting the joint formation during

the riveting process. It is also worth noting that, due to the limited number of stop positions in the interrupted experimental tests, the variation trend of the T_c was not entirely captured (Region 1 in **Fig. 14**(b)). This shortage can be easily overcome by the FE model because the T_c at any riveting stage can be conveniently extracted from the simulation results. Overall, the developed FE model of SPR process can be utilized to assist the analysis of SPR joint formation mechanisms.

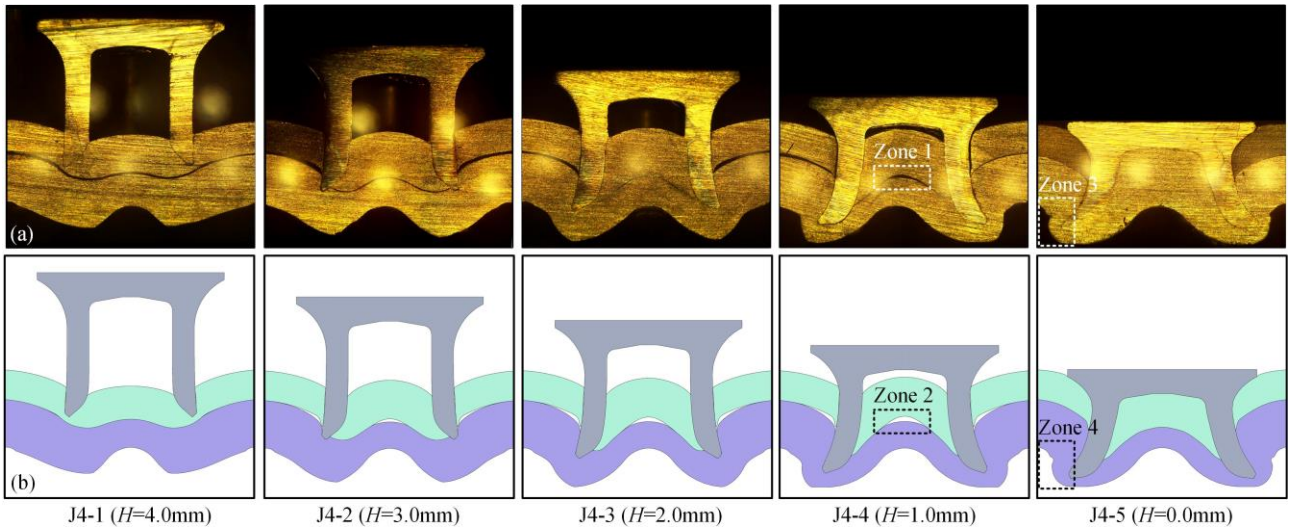

Fig. 13 Cross-sectional profiles of the joints J4-1~J4-5 from (a) the interrupted experimental tests and (b) the FE simulations

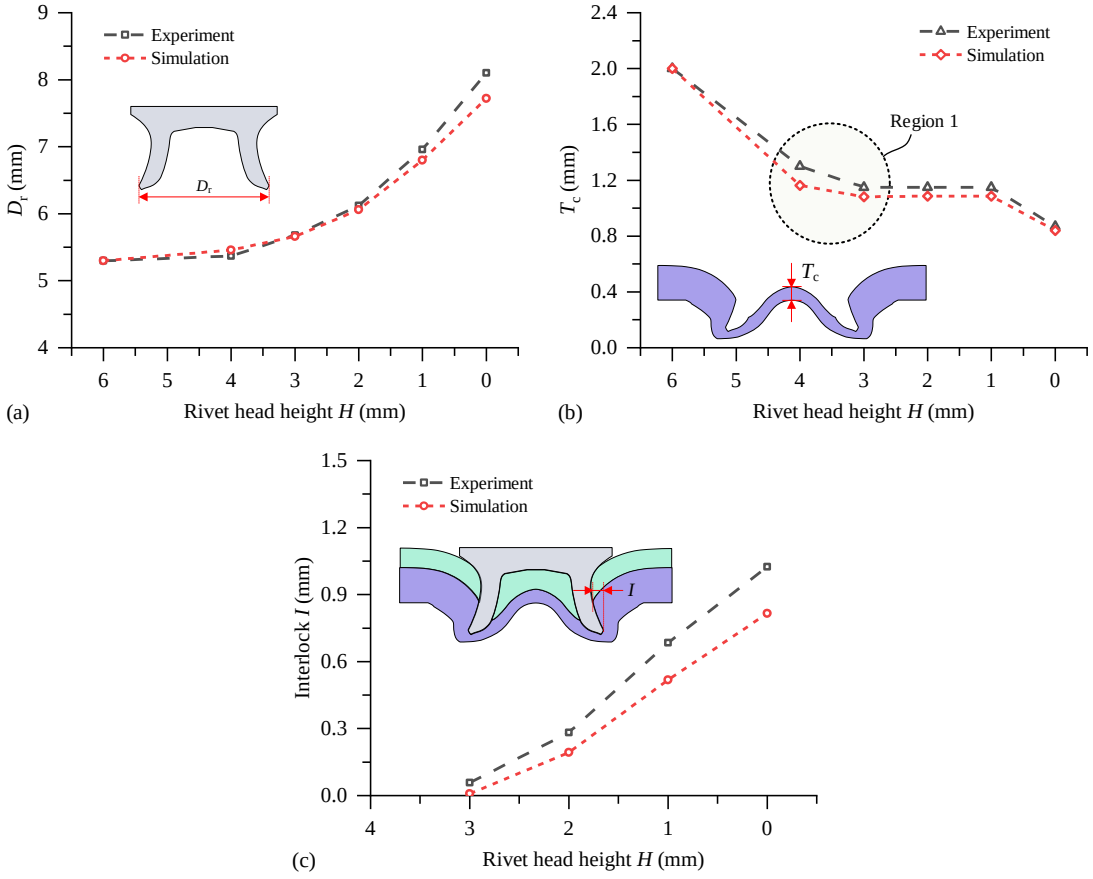

Fig. 14 Comparisons between the experimentally tested and the simulated (a) deformed rivet shank diameter D_r, (b) remaining bottom sheet thickness at the joint center T_c and (c) interlock I in the joints J4-1~J4-5

4 Results and discussions

4.1 Influences of top sheet thickness (T_t) on the joint formation mechanisms

Fig. 15 shows the experimentally captured cross-sectional profiles of the joints J1-1~J1-4 with different T_t. It can be seen that the deformed shapes of rivet and sheets were apparently influenced by the T_t, and the magnitudes of the I, T_c and T_{tip} varies from joint to joint. The tested I decreased from 0.53 mm to only 0.18 mm. As shown in **Fig. 16**, the I can be expressed as a function of the diameters of inner interlock boundary (D_{in}) and outer interlock boundary (D_{out}) (i.e., $I = (D_{out} - D_{in})/2$). It can be found that the T_t affected the interlock formation by mainly altering the inner interlock boundary: the tested D_{in} increased rapidly from 5.84 mm to 6.53 mm but the tested D_{out} only fluctuated within a narrow range (i.e., ±0.07 mm). In addition, the increment of the T_t imposed negative effects on the T_c (decreasing from 0.76 mm to 0.10 mm) but positive influences on the T_{tip} (increasing from 0.53 mm to 1.55 mm). According to the relative magnitudes of the T_c and T_{tip}, it can also be found that the minimum remaining bottom sheet thickness (T_{min}) was formed around the rivet tip with a thin top sheet (e.g., T_t=1.0 mm) but around the joint center with a thick top sheet (e.g., T_t=2.0 mm).

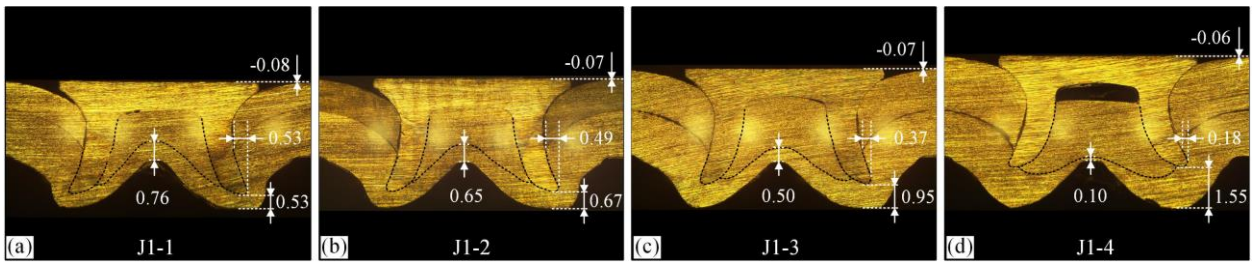

Fig. 15 Experimentally tested cross-sectional profiles of the SPR joints J1-1~J1-4: (a) T_t=1.0 mm, (b) T_t=1.2 mm, (c) T_t=1.5 mm and (d) T_t=2.0 mm

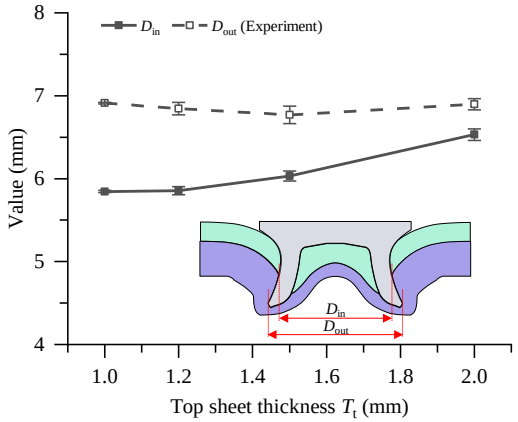

Fig. 16 Experimentally tested D_{in} and D_{out} in the SPR joints J1-1~J1-4

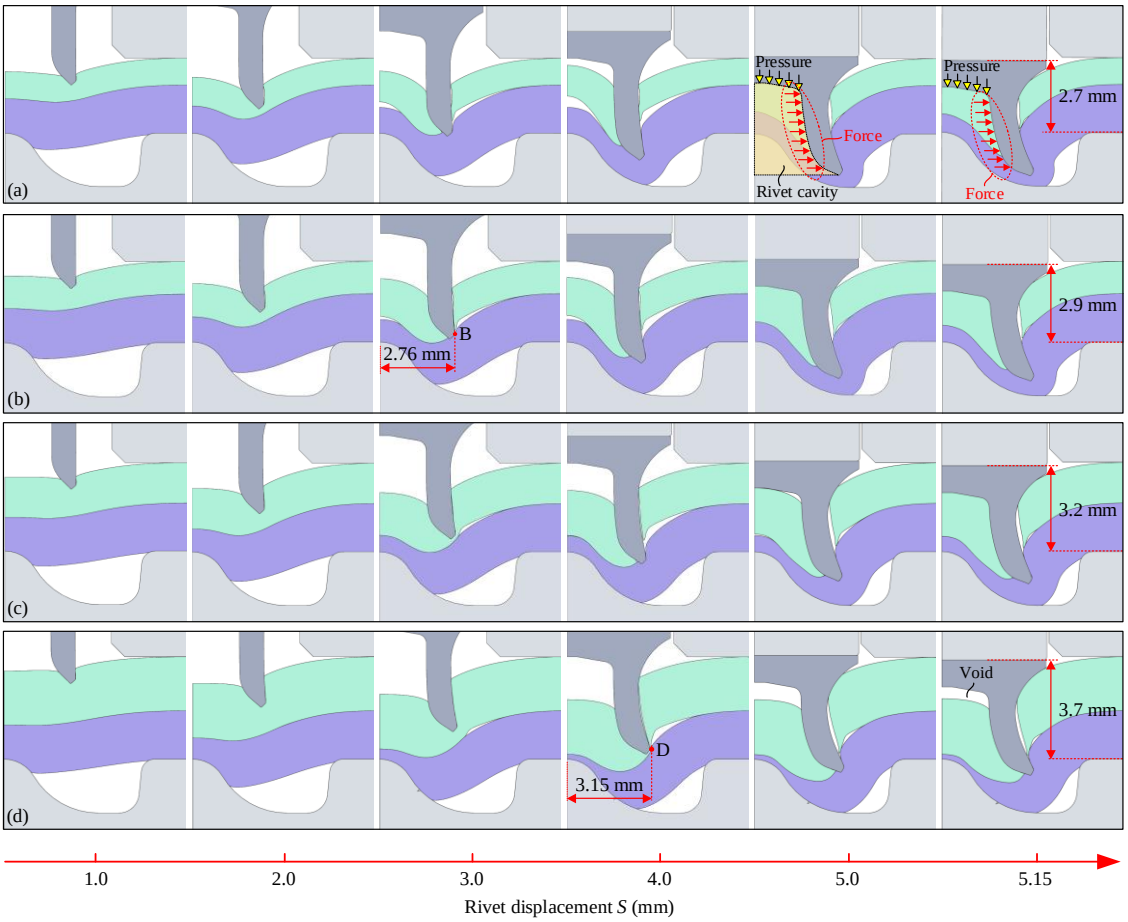

Fig. 17 Numerically simulated cross-sectional profiles during riveting processes of the SPR joints J1-1~J1-4: (a) T_t=1.0 mm, (b) T_t=1.2 mm, (c) T_t=1.5 mm and (d) T_t=2.0 mm

With the FE model, the formation processes of the SPR joints J1-1~J1-4 were visually inspected. **Fig. 17** shows the numerically extracted joint cross-sectional profiles at six different rivet displacements (S). It can be seen that, with the increment of the T_t, the top sheet became more and more difficult to be deformed. A greater rivet displacement was required before the top sheet was completely penetrated by the rivet shank. Consequently, the deformation behaviors of the rivet shank and the bottom sheet were also significantly affected, which resulted in the variations of the I, T_c and T_{tip}.

To better understand the formation mechanism of interlock with different T_t, the changing curves of the I during the riveting processes of the joints J1-1~J1-4 were numerically extracted and presented in **Fig. 18**(a). It can be seen that the starting point of interlock formation was apparently delayed with a greater T_t (Zone 1), and a smaller rivet displacement was left to form the interlock. This is mainly attributed to the delayed penetration of the thicker top sheet. Meanwhile, an equal or slightly smaller increasing speed of the I was also observed. The above changes directly caused the decline of the I with the increment of the T_t. It is worth noting that the I increased almost linearly with the increment of the rivet displacement.

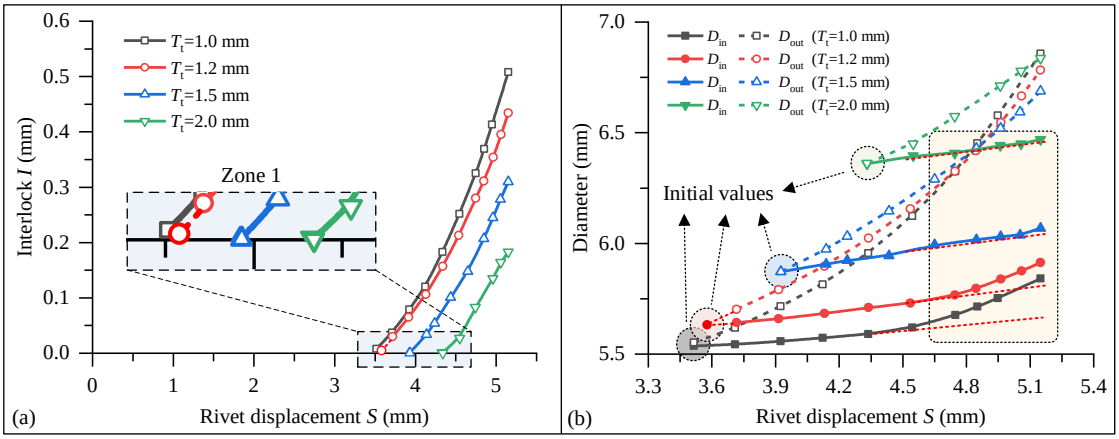

Fig. 18 Numerically simulated (a) formation curves of the I and (b) formation curves of the two interlock boundaries during riveting processes of the joints J1-1~J1-4

To find out the reasons for the different effects of the T_t on the two interlock boundaries (see **Fig. 16**), the changing curves of the D_{in} (solid lines) and D_{out} (dash lines) during the four riveting processes were numerically extracted as shown in **Fig. 18**(b). With the increment of the T_t, it can be seen that the initial values of the D_{in} and D_{out} apparently increased. This is highly associated with the insertion position where the rivet shank started flaring into the bottom sheet. As shown in **Fig. 17**, the rivet shank underwent a greater deformation when penetrating the thicker top sheet, and thus flared into the bottom sheet at a position farther away from the joint center (e.g., point B in **Fig. 17**(b) vs point D in **Fig. 17**(d)). As a result, greater initial values of the D_{in} and D_{out} were observed in the joints with a larger T_t. However, it can be seen from **Fig. 18**(b) that the increasing speed and duration of the D_{out} apparently decreased. So the initial difference of the D_{out} with varying T_t was gradually minimized, and the final value of the D_{out} was not significantly affected by the T_t. In contrast, although a shorter duration of the D_{in} was also observed with a greater T_t, the initial difference of the D_{in} with varying T_t was just slightly reduced and the final value of the D_{in} was apparently affected by the T_t. This is because different increasing speeds of the D_{in} appeared at the end of the riveting processes, and just lasted a very short period (yellow region). It is also worth mentioning that the different increasing speeds of the D_{in} were directly linked to the filling conditions of the rivet cavity. For example, the rivet cavity was fully filled before the end of the SPR process with the T_t=1.0 mm as shown in **Fig. 17**(a). With further downward movement of the rivet, the rivet head applied a high pressure on the sheet materials filled in the rivet cavity. As a result, the entire rivet shank was pushed towards the radial direction and the D_{in} experienced a faster increment speed (i.e., black solid line in **Fig. 18**(b)). In contrast, the rivet cavity was still not fully filled at the end of the SPR process with the T_t=2.0 mm as shown in **Fig. 17**(d). So the increasing speed of the D_{in} kept almost constant throughout the joining process (i.e., green solid line in **Fig. 18**(b)).

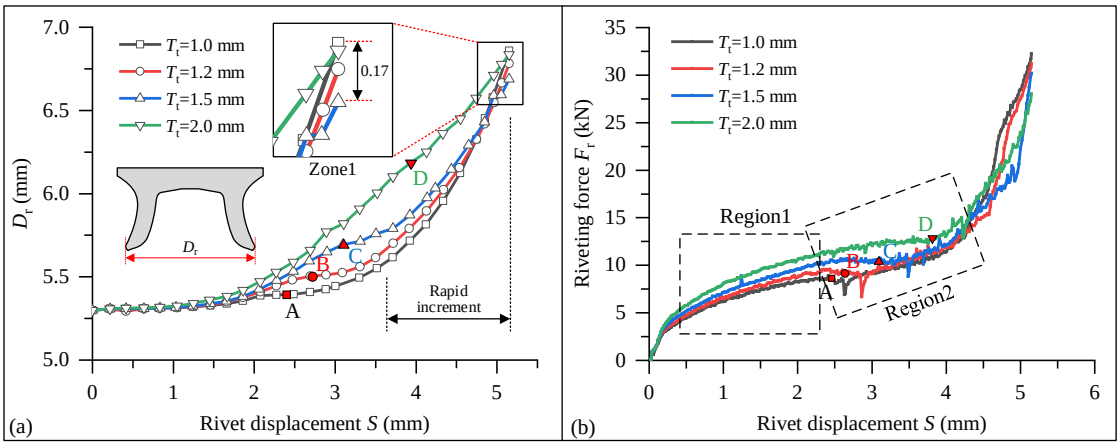

Fig. 19 Simulated (a) variation curves of the deformed rivet shank diameter (D_r) and (b) load-displacement curves in the SPR joints J1-1~J1-4 with different top sheet thicknesses

Since the flare behavior of rivet shank is vital for the interlock formation and highly associated with the resistance force that the rivet encountered, the changing curves of the deformed rivet shank diameter (D_r) and the load-displacement curves during the four joining processes were numerically extracted and analyzed as shown in **Fig. 19**. It can be seen from **Fig. 19**(a) that the four curves of the D_r demonstrated similar increment patterns but different magnitudes. The D_r always first increased slowly at the early stage, and then increased sharply until the end of the joining process. An almost constant increasing speed of the D_r was observed during the rapid increment phase. By comparing the four curves, it was also found that the slow increment of the D_r lasted for a shorter period whilst the rapid increment of the D_r lasted for a longer period in the joints with a larger T_t. This can be explained by the greater increasing speed of the riveting force (F_r) at the early stage of the joining process with a larger T_t (Region1 in **Fig. 19**(b)), which resulted in a higher F_r and thus an earlier start of the rapid increment phase of the D_r. However, due to the slightly smaller rapid increasing speed of the D_r, the maximum value of the D_r was not significantly affected by the T_t (Zone1 in **Fig. 19**(a)). The points A, B, C and D in **Fig. 19**(a) indicate the positions where the top sheet was penetrated by the rivet shank. It can be seen that the increment speed of the D_r was negatively affected by the separation/fracture of the 1.0 mm, 1.2 mm and 1.5 mm top sheets (points A, B, C), but almost not influenced by the fracture of the 2.0 mm top sheet (point D). This might be attributed to the slow increment of the F_r around the points A, B, C but the immediate sharp increment of the F_r following the point D (Region2 in **Fig. 19**(b)). With the T_t=1.0 mm, the D_r just increased a limited value before the top sheet was penetrated at the point A (i.e., black line). The major growth of the D_r mainly occurred after the rivet shank flared into the bottom sheet. In contrast, with the T_t=2.0 mm (i.e., green line), a large increment of the D_r was observed before the top sheet was penetrated at the point D, whilst a smaller increment of the D_r was observed after the rivet shank flared into the bottom sheet. Overall, the flare behavior of the rivet shank can be significantly influenced by the T_t.

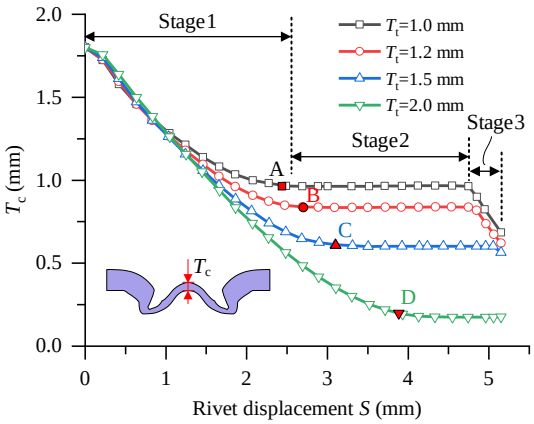

Fig. 20 Simulated variation curves of the T_c with different top sheet thicknesses T_t

To understand the formation mechanism of the T_c with different T_t, the changing curves of the T_c during the four riveting processes were numerically extracted as shown in **Fig. 20**. It can be seen that the T_c on the four curves underwent three different decline stages: it first decreased rapidly (Stage1), and then kept almost constant for a period (Stage2) before the second rapid decline occurred (Stage3). The Stage1 started at the beginning of the riveting process, and ended after the top sheet was completely penetrated by the rivet shank (points A, B, C and D). The fracture of top sheet directly changed the magnitudes of stresses distributed around the center of the bottom sheet, which terminated the rapid decline of the T_c. For instance, **Fig. 21**(a) shows the equivalent stress distribution on the bottom sheet of the joint J1-1 before and after the top sheet separation. Quite large stresses were found around the center of the bottom sheet before the top sheet was penetrated (Zone1), but relatively small stresses were found around the same region after the fracture of the top sheet (Zone2). With the increment of the T_t, the length of the Stage1 apparently increased because a larger rivet displacement was required before the top sheet was penetrated. It can also be found that the decreasing speed of the T_c was less influenced by the T_t and remained almost constant at the Stage1. During the Stage2, the stresses around the center of the bottom sheet maintained at a relatively low level, and thus the decreasing speed of the T_c equaled to almost zero. Once the rivet cavity was fully filled with the top sheet material, the Stage3 started and the T_c rapidly decreased again. This is because the rivet head applied a high pressure on the sheet material trapped in the rivet cavity, and the stresses around the center of the bottom sheet increased to a high level. For instance, **Fig. 21**(b) shows the equivalent stress distribution on the bottom sheet of the joint J1-1 before and after the rivet cavity was fully filled. The relatively small stresses in Zone3 and the large stresses in Zone4 clearly explained the appearance of the Stage3. With the increment of the T_t, the length of the Stage3 apparently decreased or even disappeared. This is because the filling of the rivet cavity was apparently delayed with a greater T_t as shown in **Fig. 17**. Furthermore, the increment of the T_t directly increased the distance from the final position of the rivet to the bottom of the die cavity as shown in **Fig. 17**, which caused the increasing trend of the T_{tip}. It is also worth noting that the increment of the T_{tip} is almost equal to the increment of the T_t. This can be explained by the similar magnitudes of the final rivet shank diameter (D_r).

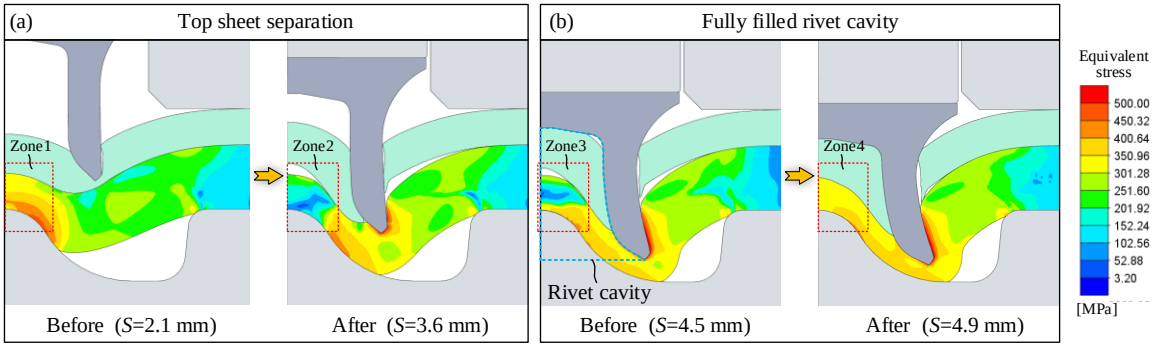

Fig. 21 Equivalent stress distribution on the bottom sheet of the joint J1-1 (T_t=1.0 mm): (a) before and after top sheet separation and (b) before and after the fully filled rivet cavity

4.2 Influences of bottom sheet thickness (T_b) on the joint formation mechanisms

Fig. 22 presents the experimentally captured cross-sectional profiles of the joints J2-1~J2-4 with different T_b. It can be seen that the top and bottom sheets underwent less plastic deformation with the increment of the T_b. The rivet shank also flared a smaller distance towards the radial direction. The large gaps formed between the two sheets and formed between the rivet head and the top sheet in the joint J2-1 were almost eliminated in the joint J2-4 (Zone1 in **Fig. 22**(d)). The tested I increased from 0.23 mm to 0.53 mm with the increment of the T_b. **Fig. 23** shows the variations of the two interlock boundaries with varying T_b. Different form the T_t, the T_b affected the interlock formation by altering the two interlock boundaries: the tested D_{in} declined from 7.06 mm to 5.66 mm and the tested D_{out} decreased from 7.48 mm to 6.72 mm. The greater reduction of the D_{in} compared to the D_{out} directly caused the increment of the I. Moreover, the increment of the T_b also showed positive influences on the T_c (increasing from 0.42 mm to 0.69 mm) and T_{tip} (increasing from 0.23 mm to 0.53 mm). According to the relative magnitudes of the T_c and T_{tip}, it can also be found that the T_{min} was formed around the rivet tip with a thin bottom sheet (e.g., T_b=1.0 mm) but around the joint center with a thick bottom sheet (e.g., T_b=2.0 mm).

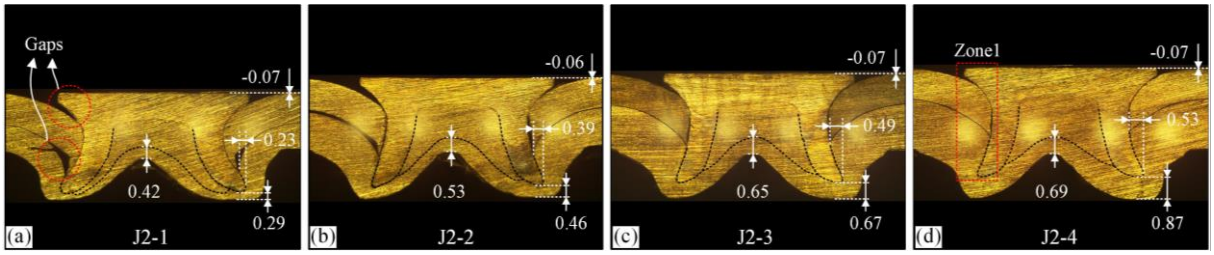

Fig. 22 Experimentally tested cross-sectional profiles of the SPR joints J2-1~J2-4: (a) T_b=1.0 mm, (b) T_b=1.5 mm, (c) T_b=1.8 mm and (d) T_b=2.0 mm

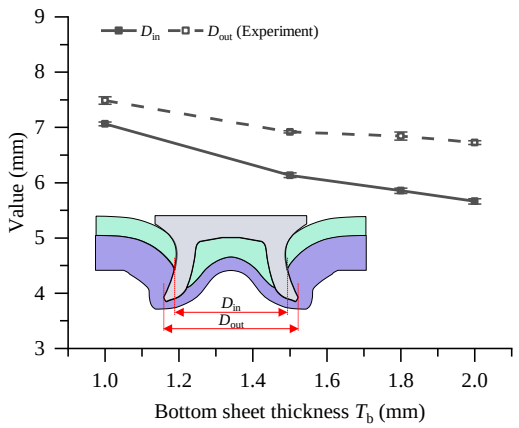

Fig. 23 Experimentally tested D_{in} and D_{out} in the SPR joints J2-1~J2-4

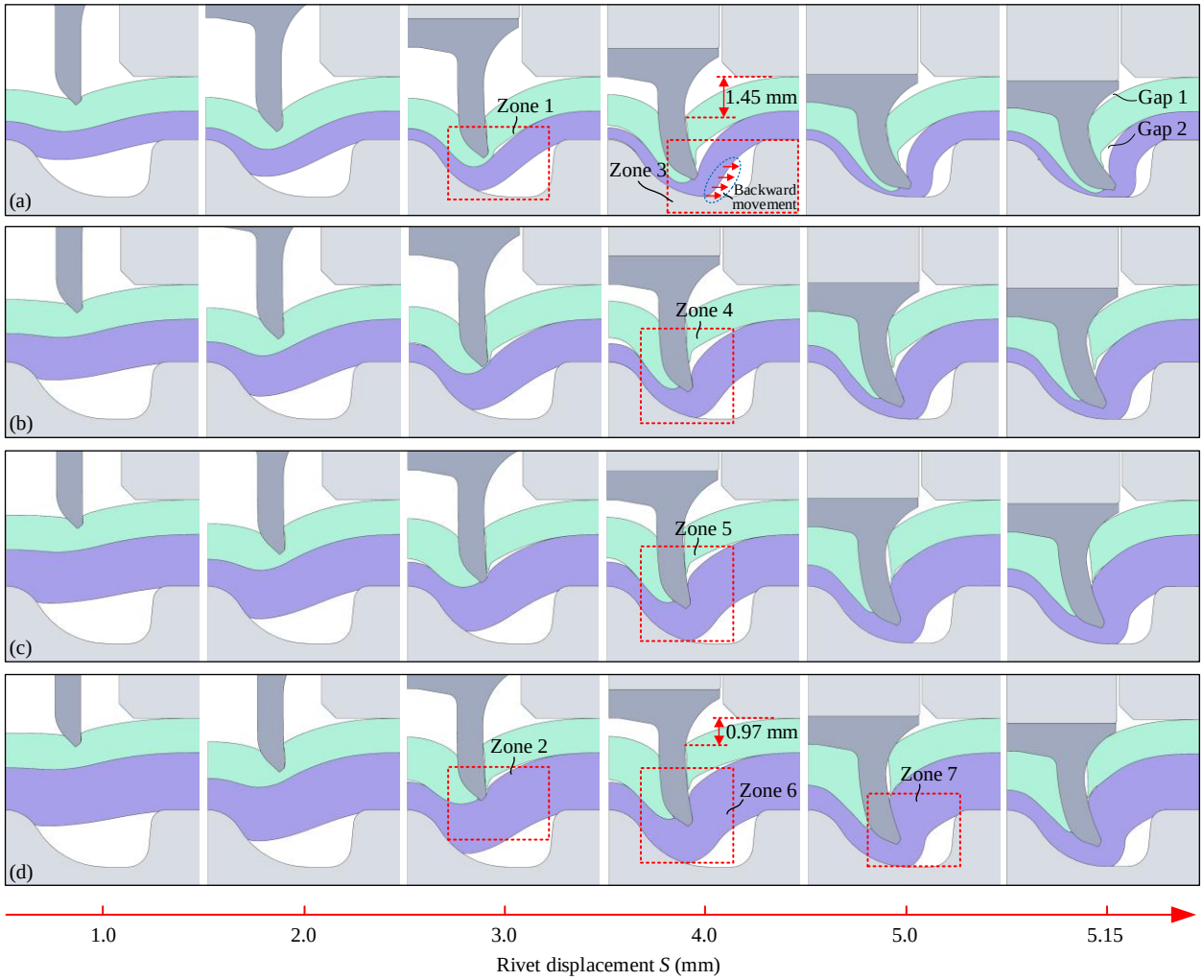

Fig. 24 Numerically simulated cross-sectional profiles during the riveting processes of the SPR joints J2-1~J2-4: (a) T_b=1.0 mm, (b) T_b=1.5 mm, (c) T_b=1.8 mm and (d) T_b=2.0 mm

To visually inspect the formation mechanism of the joints J2-1~J2-4, the joint cross-sectional profiles at six different rivet displacements (S) of each riveting process were numerically extracted as shown in **Fig. 24**. By comparing the deformation behavior of the bottom sheet, it can be found that the increment of the T_b apparently made the bottom sheet more difficult to be deformed. Correspondingly, the downward movement of the top sheet was apparently restricted. For instance, when the S=4.0 mm, the top sheet underwent a 1.45 mm downward displacement with the T_b=1.0 mm in **Fig. 24**(a) but a 0.97 mm downward displacement with the T_b=2.0 mm in **Fig. 24**(d). The smaller downward displacement of the top sheet and the smaller backward movement of the bottom sheet effectively avoided the formation of gaps appeared in the final joints (e.g., Gap 1 and Gap 2 in **Fig. 24**(a) vs no gap in **Fig. 24**(d)). This indicates that a tightly connected joint is more likely formed with a thicker bottom sheet than with a thinner one.

To uncover the impact of the T_b on the interlock formation, the changing curves of the I during the four riveting processes were numerically extracted as shown in **Fig. 25**(a). It can be seen that, with the increment of the T_b, the interlock formation started at an earlier time (Zone 1). This is because the thicker bottom sheet provided a greater resistance force on the top sheet, which allowed the top sheet to be penetrated by the rivet shank at a

faster speed rather than to be pressed downward rapidly (e.g., Zone 1 vs Zone 2 in **Fig. 24**). The rivet shank started flaring into the bottom sheet at an earlier time, and therefore the interlock formation also occurred at an earlier time. Moreover, similar increasing speeds of the I were observed on the four curves, whilst the interlock formation process lasted for a longer period when with a thicker bottom sheet. As a result, the I showed an increasing trend with the increment of the T_b.

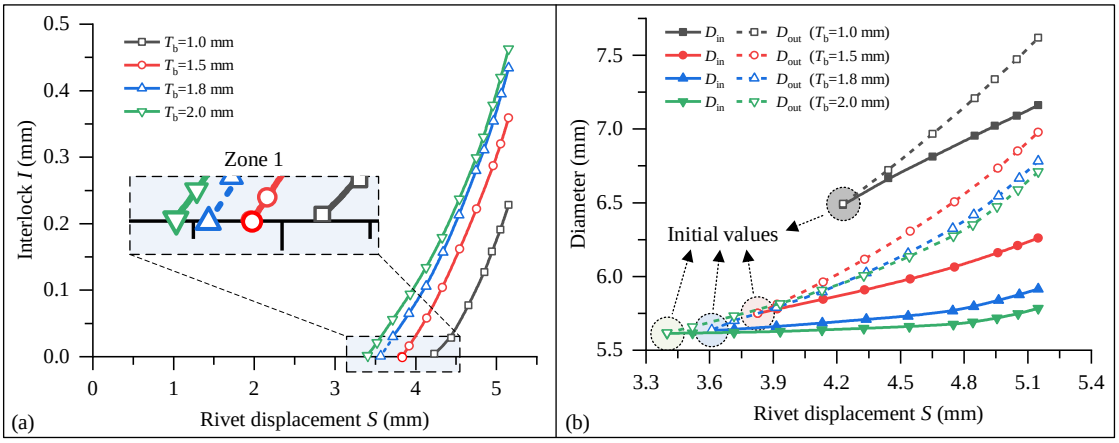

Fig. 25 Numerically simulated (a) formation curves of the I and (b) formation curves of the two interlock boundaries during riveting processes of the joints J2-1~J2-4

Fig. 25(b) shows the numerically extracted changing curves of the D_{in} (solid lines) and D_{out} (dash lines) during the four riveting processes. It can be seen that the initial values of the D_{in} and D_{out} apparently decreased with the T_b increasing from 1.0 mm to 1.5 mm (marked with black and red circles), but just slightly decreased with the T_b increasing from 1.5 mm to 2.0 mm (marked with red, blue and green circles). This can be explained by the different rigidities of bottom sheets with varying T_b. Compared with the 1.5 mm, 1.8 mm and 2.0 mm bottom sheets, the 1.0 mm bottom sheet had a much lower rigidity and thus was easily pushed backward rather than pierced by the rivet shank after the completely penetration of the top sheet (Zone 3 in **Fig. 24**(a)). As a result, the rivet shank started flaring into the bottom sheet at a very late time, and the initial values of the D_{in} and D_{out} were apparently greater than that in other three joints. In contrast, the rigidity of the 1.5 mm bottom sheet was already large enough to avoid fast backward movement of the bottom sheet. The increment of the T_b from 1.5 mm to 2.0 mm further restricted the backward movement of the bottom sheet, and led to a slightly earlier start of the rivet shank flaring into the bottom sheet. Due to the similarly limited rivet shank deformation in the three riveting processes (Zone 4, Zone 5 and Zone 6 in **Fig. 24**(b)(c)(d)), the initial values of the D_{in} and D_{out} just slightly changed. From **Fig. 25**(b), it can be also found that the increasing speed of the D_{in} showed a decreasing trend with the increment of the T_b. Similar phenomenon was also observed for the increasing speed of the D_{out}. As a result, the initial differences of the D_{in} and D_{out} during the four riveting processes could not be eliminated and therefore both of the D_{in} and D_{out} showed a decreasing tendency with the increment of the T_b as shown in **Fig. 23**.

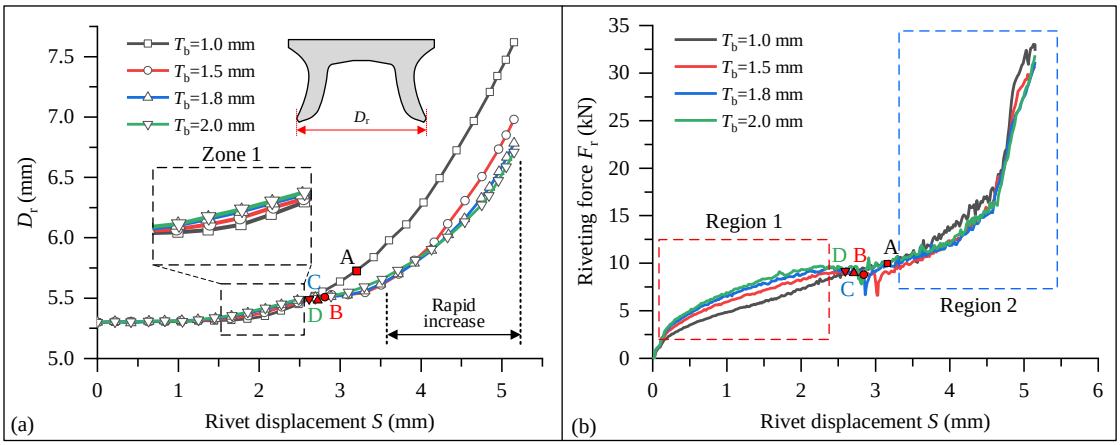

Fig. 26 Simulated (a) variation curves of the deformed rivet shank diameter (D_r) and (b) load-displacement curves in the SPR joints J2-1~J2-4 with different bottom sheet thicknesses

Fig. 26(a) shows the numerically extracted changing curves of the deformed rivet shank diameter (D_r) during the four joining processes. It can be seen that the flare behavior of rivet shank was apparently affected by the T_b. Before the top sheet was completely penetrated by the rivet shank (marked as points A, B, C and D), the D_r on the four curves increased slowly and its magnitude just increased a little bit with the increment of the T_b (Zone 1). This is attributed to the slightly greater riveting force (Region 1 in **Fig. 26**(b)) induced by the higher rigidity of the thicker bottom sheet. Obvious difference between the four curves was observed after the penetration of the top sheet. Although similar magnitudes of the F_r were observed during this period (Region 2 in **Fig. 26**(b)), the increasing speed of the D_r demonstrated a decreasing trend with the increment of the T_b. This is also because the thicker bottom sheet is increasingly difficult to be pushed backward. The rivet shank was inserted into the thicker bottom sheet quickly along the vertical direction rather than along the radial direction. As a result, the maximum D_r showed a decreasing trend with the increment of the T_b. From the above analyses, it can be concluded that the increment of the T_b had negative effects on the rivet shank flaring under the studied joint configurations.

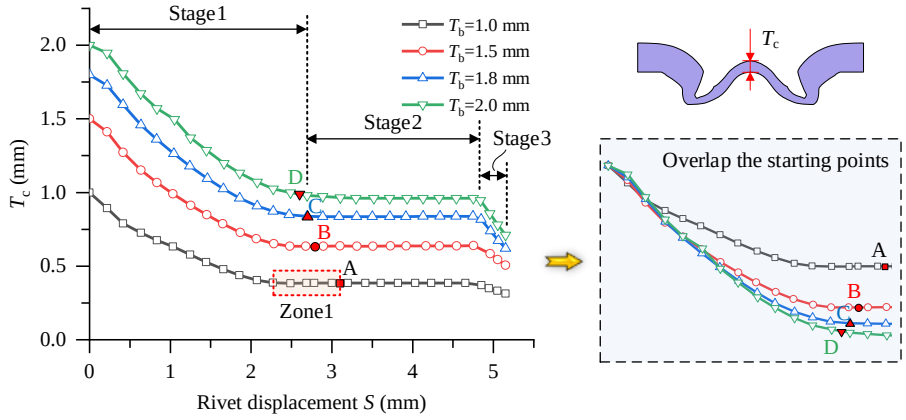

Fig. 27 Simulated variation curves of the T_c with different bottom sheet thicknesses T_b

To figure out the impact of the T_b on the formation of the T_c, the numerically extracted changing curves of the T_c during the four riveting processes are presented in **Fig. 27**. For easier comparison, the starting points of the four curves were overlapped together. It can be seen that the lengths of the first rapid decrease (i.e., Stage1) were almost the same on the four curves. However, with the increment of the T_b, the T_c reduced a greater value

during this stage. It was also noticed that the Stage1 stopped before the top sheet was completely penetrated with T_b=1.0 mm in the joint J2-1 (point A on the black line). This is attributed to the changes of the stress distribution around the central area of the bottom sheet. As shown in **Fig. 28**, quite high stresses were observed on the bottom sheet when the rivet displacement equaled to 2.1 mm (Zone 1), but the magnitudes of stresses reduced to a low level when the rivet displacement increased to 2.7 mm (Zone 2). The earlier reduction of the stresses was directly caused by the large deformation of the low rigidity 1.0 mm top sheet. Moreover, by comparing the four curves, it can also be seen that the second rapid decrease (i.e., Stage3) started almost at the same time. This is because the T_b showed limited influences on the filling condition of the rivet cavity. However, a greater decreasing speed of the T_c was found with a thicker bottom sheet during this stage. This might be explained by the larger amount of bottom sheet material and the lower-level equivalent strains around the center of the thicker bottom sheet (e.g., Zone 1 and Zone 2 in **Fig. 29**). Finally, although the T_c reduced greater values during the Stage1 and Stage3, the final magnitude of the T_c still showed an increasing trend with the increment of the T_b.

Furthermore, similarly to the T_t, the increment of the T_b also significantly increased the distance from the final position of the rivet to the bottom of the die cavity, and thus caused the increment of the T_{tip}. It is worth mentioning that the increased value of the T_{tip} is smaller than the increment of the T_b. This can be explained by the reduction of the rivet shank flare with a thicker bottom sheet.

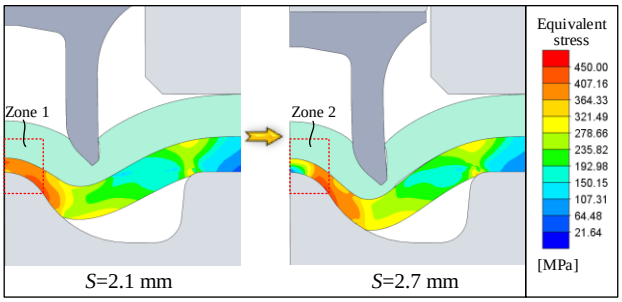

Fig. 28 Equivalent stress distribution on the bottom sheet of the joint J2-1 (T_b=1.0 mm)

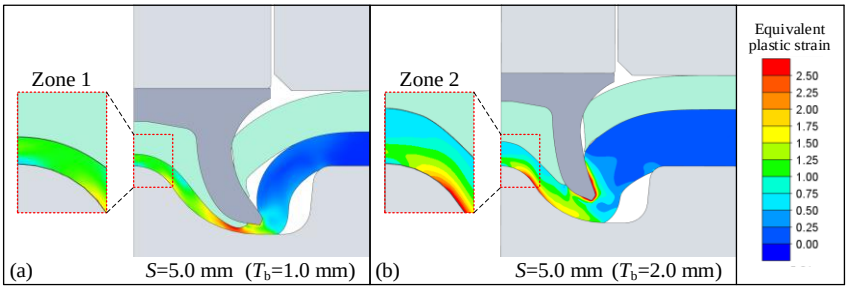

Fig. 29 Equivalent plastic strain distribution on the bottom sheet of the (a) joint J2-1 and (b) joint J2-4

4.3 Influences of rivet length (*L*) on the joint formation mechanisms

Fig. 30 shows the experimentally captured cross-sectional profiles of the joints J3-1~J3-3 with different *L*. It can be seen that the final joint profiles were also significantly affected by the *L*, especially the deformed bottom sheet around the rivet tip. With the increment of the *L*, the tested *I* rapidly increased from 0.49 mm to 1.23 mm. **Fig. 31** shows the variations of the two interlock boundaries. It can be found that the *L* affected the interlock formation by mainly altering the outer interlock boundary: the D_{out} increased rapidly from 6.84 mm to 8.48 mm

but the D_{in} just slightly increased from 5.85 mm to 6.03 mm. The increment of the L imposed negative effects on the T_{tip} (decreasing from 0.67 mm to 0.26 mm) but limited influences on the T_c (fluctuating within 0.65~0.71 mm). According to the relative magnitudes of the T_c and T_{tip}, it can also be found that the T_{min} was formed around the joint center with a short rivet (e.g., L=5.0 mm) but around the rivet tip with a long rivet (e.g., L=6.5 mm).

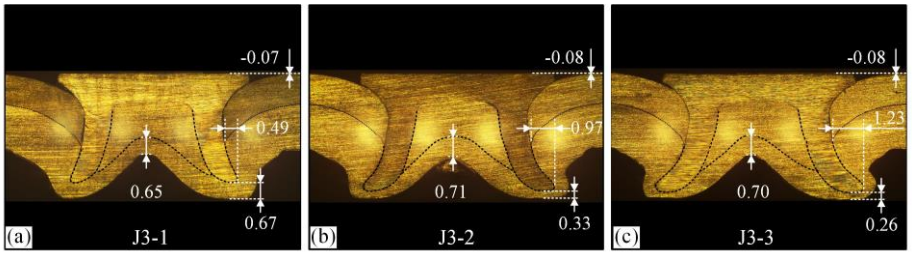

Fig. 30 Experimentally tested cross-sectional profiles of the SPR joints J3-1~J3-3: (a) L=5.0 mm, (b) L=6.0 mm, (c) L=6.5 mm

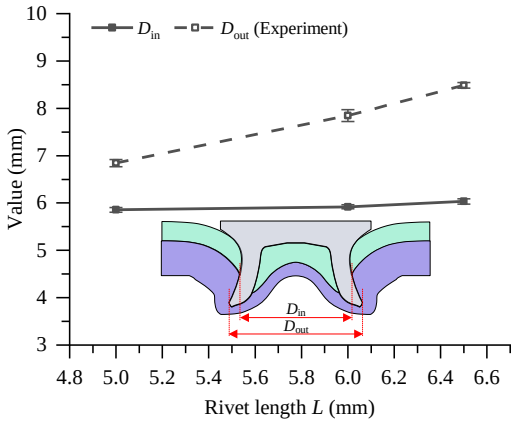

Fig. 31 Experimentally tested D_{in} and D_{out} in the SPR joints J3-1~J3-3

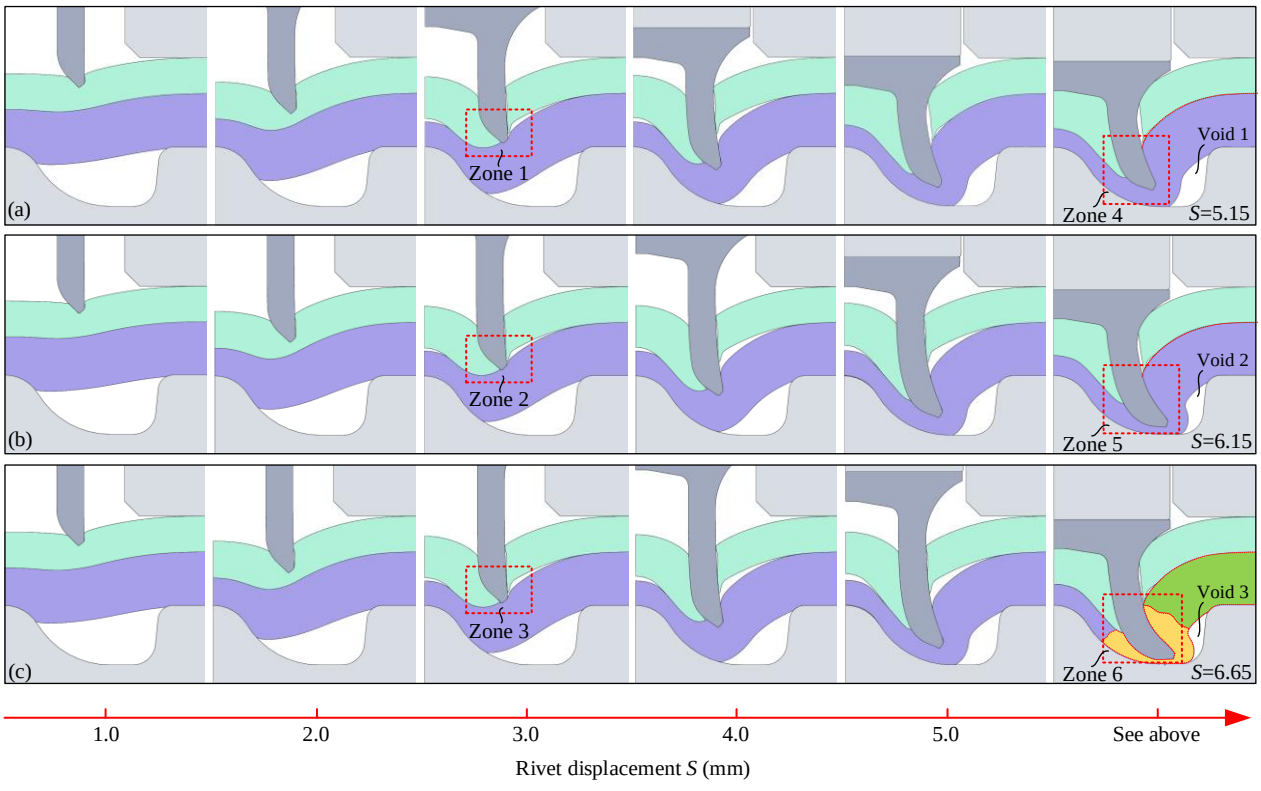

Fig. 32 Numerically simulated cross-sectional profiles during riveting processes of the SPR joints J3-1~J3-3: (a) L=5.0 mm, (b) L=6.0 mm and (c) L=6.5 mm

With the help of the FE model, the joint cross-sectional profiles at six different rivet displacements (S) were numerically extracted to observe the joint formations with different L as shown in **Fig. 32**. Before the head of the 5.0 mm long rivet started pressing the top sheet (S≈4.0 mm), it can be seen that the deformed shapes of the top and bottom sheets during the three riveting processes were almost identical. The penetration of the top sheet was not obviously affected by the L and occurred at almost the same time (Zones 1, 2 and 3). Major differences were observed at the later stage of these joining processes. The rivet shank apparently flared a larger distance into the bottom sheet with the increment of the L (Zones 4, 5 and 6). As a result, a greater localized deformation of the bottom sheet was found around the rivet tip (yellow region in **Fig. 32**(c)), whilst the final shape of the bottom sheet far from the rivet tip (green and violet regions in **Fig. 32**(c)) remained almost the same in the three joints. Consequently, the final magnitudes of the quality indicators I, T_c and T_{tip} were affected to different degrees.

Fig. 33(a) shows the impact of the L on the interlock formation process. It can be seen that the starting point of interlock formation was nearly the same (Zone 1), and the increasing speed of the I was almost identical on the three curves. The only difference is that the quick increase of the I lasted for a longer period with the increment of the L. With the increment of the rivet displacement, the nearly same increasing patterns and magnitudes of the I on the three curves explained the linear increment of the final I.

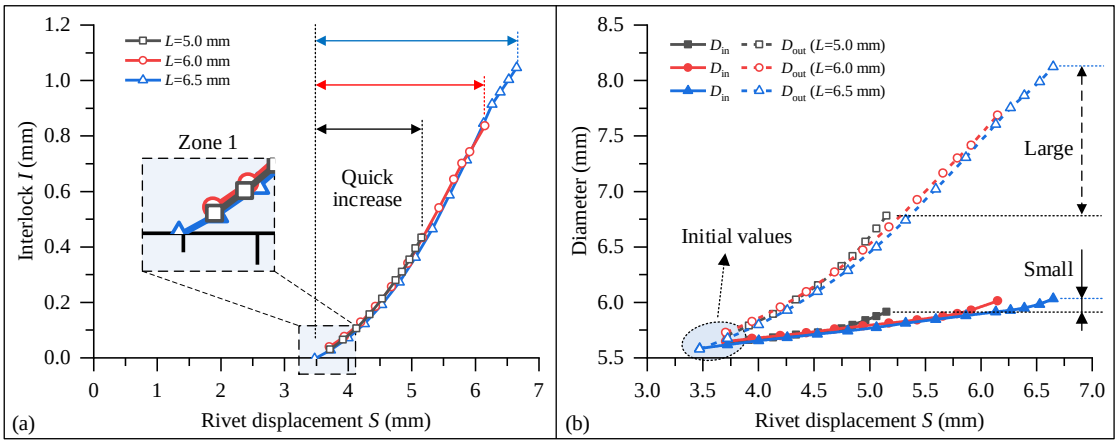

Fig. 33 Numerically simulated (a) formation curves of the I and (b) formation curves of the two interlock boundaries during riveting processes of the joints J3-1~J3-3

Fig. 33(b) shows the numerically extracted changing curves of the D_{in} (solid lines) and D_{out} (dash lines) during the three riveting processes. It can be seen that the D_{in} experienced a similar increasing pattern but lasted for a longer period with the increment of the L. Similar phenomenon was also identified from the three changing curves of the D_{out}. The large enough space of the die cavity successfully accommodated the materials of sheets and rivets with varying L, and contributed to the similar increasing patterns of the D_{in} and D_{out}. However, due to the relatively low increasing speed of the D_{in}, the maximum D_{in} increased a limited value with the L increasing from 5.0 mm to 6.5 mm. In contrast, because of the high increment speed of the D_{out}, the maximum D_{out} increased a quite large value with the increment of the L. The increasing patterns of these curves clearly uncovered the different influences of the L on the two interlock boundaries shown in **Fig. 31**. Overall, the L affected the interlock formation by mainly altering the position of the outer interlock boundary under the studied joint configurations.

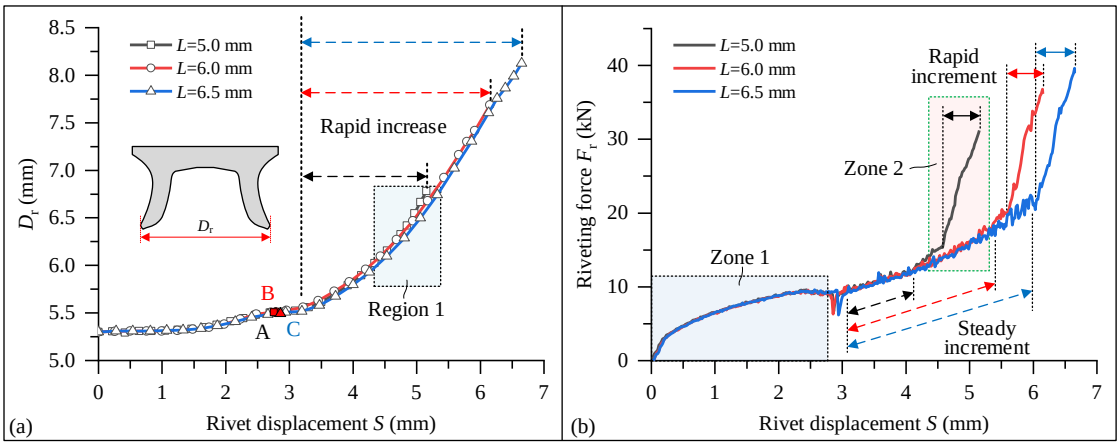

Fig. 34 Simulated (a) variation curves of the deformed rivet shank diameter (D_r) and (b) load-displacement curves in the SPR joints J3-1~J3-3 with different rivet lengths

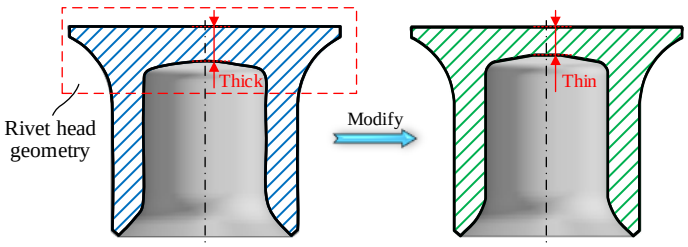

Fig. 35 Modification of the rivet head geometry to reduce the maximum riveting force

The numerically extracted changing curves of the deformed rivet shank diameter (D_r) during the three riveting processes are shown in **Fig. 34**(a). It can be seen that the magnitudes of the D_r were almost the same at the slow increment stage on the three curves. This can be explained by the same riveting forces (F_r) during this period (Zone 1 in **Fig. 34**(b)). The increasing speeds of the D_r at the rapid increase stage were nearly identical on the three curves. Compared with the steady increment of the F_r with the L=6.0 mm and 6.5 mm (Zone 2 in **Fig. 34**(b)), the F_r with L=5.0 mm experienced a much faster increment but contributed very little to the rivet shank flare (Region 1 in **Fig. 34**(a)). This is because a large part of the F_r was used to overcome the resistance force applied on the rivet head instead of that applied on the rivet shank. This phenomenon indicates that, by properly optimizing the rivet head geometry, it might be possible to reduce the maximum riveting force without affecting too much of the rivet shank flare behavior. For example, the occurrence of the rapid increment of the F_r can be delayed by reducing the thickness around the central area of the rivet head (see **Fig. 35**), and therefore the maximum riveting force can decrease to a smaller value. As shown in **Fig. 34**(a), the main difference between the three curves is that the rapid increment of the D_r lasted for a longer period with a greater L. This directly caused the almost linear increment trends of the I and the D_{out} shown in **Fig. 30**. By comparing the three load-displacement curves in **Fig. 34**(b), it is also found that the increment of the L led to a larger length of the steady increment of the F_r, but showed little influence on the increasing pattern and speed at the rapid increment stage of the F_r. In general, the L had significant influences on the flare behavior of the rivet shank.

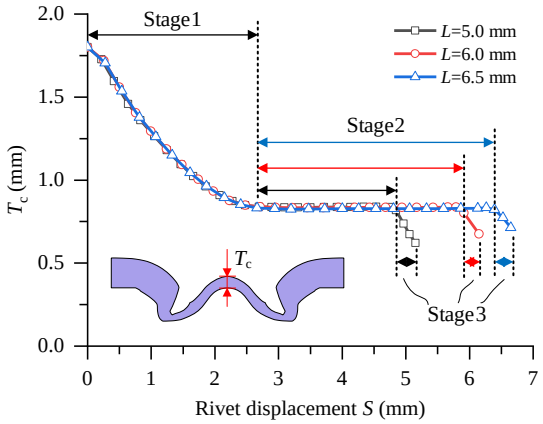

Fig. 36 Simulated variation curves of the T_c with different rivet lengths L

Fig. 36 shows the influences of the L on the formation of the T_c. By comparing the three changing curves of the T_c, it can be found that the increment of the L had no influence on the speed and length of the first rapid decrease of the T_c (i.e., Stage1). However, it led to a longer length of the Stage2 and delayed the appearance of the second rapid decrease of the T_c (i.e., Stage3). During the Stage3, a slightly smaller decreasing speed of the T_c was observed with a larger L. This difference might be attributed to the different filling conditions of the die cavity. With the increment of the L, the decreasing void space in the die cavity (i.e., Void 1> Void 2>Void 3 in **Fig. 32**) restricted the deformations of the rivet and bottom sheet, and thus led to the slightly smaller speed of the T_c. As a result, the increment of the L imposed very limited influences on the maximum T_c. Moreover, the increment of the L directly shortened the relative distance between the final position of the rivet tip and the die as shown in **Fig. 32**, and therefore caused the rapid decline of the T_{tip} shown in **Fig. 30**.

From the above analyses of joint formation processes with varying T_t, T_b and L, it can be found that the FE model of SPR process is a very powerful tool for the investigation of joining parameters' impact on the SPR joint formation. Information within the joining region can be easily extracted with the FE model to inspect the events happened during the riveting process. This makes the analysis of experimental results much easier and more intuitive. By linking the deformation behaviors of the rivet and sheets with the joint quality indicators, the formation mechanism of the SPR joint can be clearly understood. Therefore, the FE model has great potentials to become a mainstream research approach to speed up the development of SPR technique.

5 Conclusions

In this study, single factor experimental SPR tests combined with a verified FE model were utilized to investigate the formation mechanisms of SPR joints with varying T_t, T_b and L. The main conclusions are summarized below:

(1) The T_t, L and T_b imposed significant influences on the interlock formation by altering the position of the inner interlock boundary, the position of the outer interlock boundary and the two interlock boundaries (inner and outer) respectively.

(2) The formation of T_c was negatively affected by the increment of the T_t, positively influenced by the increment of the T_b, but rarely affected by the increment of the L. The rapid decline of T_c mainly occurred before the top sheet was completely penetrated and after the rivet cavity was fully filled. The formation of T_{tip} was positively

influenced by the increments of the T_t and T_b, but negatively affected by the increment of the L. The T_{min} was more likely formed around the joint center with the increment of the T_t or T_b, but around the rivet tip with the increment of the L.

(3) When piercing through the top sheet, the rivet shank flare behavior was significantly affected by the T_t, but just slightly affected by the T_b and L. When flaring into the bottom sheet, the flare speed of the rivet shank decreased with the increment of the T_t and T_b, but remained almost constant with the increment of the L. the final value of D_r fluctuated in a narrow range with the increment of the T_t, apparently decreased with the increment of the T_b, but increased almost linearly with the increment of the L.

(4) The FE model is an excellent alternative of the interrupted experimental test to study the SPR joint formation mechanisms. The deformation behaviors of rivet and sheets, the changing trend of riveting force and the formation process of joint quality indicators can be accurately predicted.

CRediT authorship contribution statement

Huan Zhao: Methodology, Writing-original draft, Writing-review & editing, Investigation. **Li Han**: Supervision, Writing-review & editing. **Yunpeng Liu**: Methodology, Writing-review & editing, Investigation. **Xianping Liu**: Supervision, Project administration, Funding acquisition.

Declaration of competing interest

The authors declare that they have no known competing financial interests or personal relationships that could have appeared to influence the work reported in this paper.

Acknowledgements

This research is funded by Jaguar Land Rover. The authors would like to thank Dr. Matthias Wissling, Paul Bartig and their team members from Tucker GmbH for their supports during the laboratory tests.

References

[1] Reinhert P. The new Jaguar XJ - The first all aluminium car in monocoque design. Alum Int Today 2004;16:21–4.

[2] Zhao H, Han L, Liu Y, Liu X. Quality prediction and rivet/die selection for SPR joints with artificial neural network and genetic algorithm. J Manuf Process 2021;66:574–94. https://doi.org/10.1016/j.jmapro.2021.04.033.

[3] Abe Y, Maeda T, Yoshioka D, Mori KI. Mechanical clinching and self-pierce riveting of thin three sheets of 5000 series aluminium alloy and 980 MPa grade cold rolled ultra-high strength steel. Materials (Basel) 2020;13:1–22. https://doi.org/10.3390/ma13214741.

[4] Ma Y, Shan H, Niu S, Li Y, Lin Z, Ma N. A comparative study of friction self-piercing riveting and self-piercing

riveting of aluminum alloy AA5182-O. Engineering 2020. https://doi.org/10.1016/J.ENG.2020.06.015.

[5] Ma Y, Niu S, Liu H, Li Y, Ma N. Microstructural evolution in friction self-piercing riveted aluminum alloy AA7075-T6 joints. J Mater Sci Technol 2021;82:80–95. https://doi.org/10.1016/J.JMST.2020.12.023.

[6] Jiang H, Gao S, Li G, Cui J. Structural design of half hollow rivet for electromagnetic self-piercing riveting process of dissimilar materials. Mater Des 2019;183:108141. https://doi.org/10.1016/j.matdes.2019.108141.

[7] Lou M, Li Y, Li Y, Chen G. Behavior and quality evaluation of electroplastic self-piercing riveting of aluminum alloy and advanced high strength steel. J Manuf Sci Eng Trans ASME 2013;135. https://doi.org/10.1115/1.4023256.

[8] Deng L, Lou M, Li Y, Carlson BE. Thermally assisted self-piercing riveting of AA6061-T6 to ultrahigh strength steel. J Manuf Sci Eng Trans ASME 2019;141. https://doi.org/10.1115/1.4044255.

[9] Haque R. Quality of self-piercing riveting (SPR) joints from cross-sectional perspective: A review. Arch Civ Mech Eng 2018;18:83–93. https://doi.org/10.1016/j.acme.2017.06.003.

[10] Liu Y, Han L, Zhao H, Liu X. Evaluation and correction of cutting position's effects on quality indicator measurement of self-piercing riveted joint. Mater Des 2021:109583. https://doi.org/10.1016/J.MATDES.2021.109583.

[11] Han L, Thornton M, Li D, Shergold M. Effect of setting velocity on self-piercing riveting process and joint behaviour for automotive applications. SAE Tech Pap 2010. https://doi.org/10.4271/2010-01-0966.

[12] Kam DH, Jeong TE, Kim MG, Shin J. Self-piercing riveted joint of vibration-damping steel and aluminum alloy. Appl Sci 2019;9:4575. https://doi.org/10.3390/app9214575.

[13] Li D, Han L, Chrysanthou A, Shergold M. Influence of corrosion of self-piercing riveted high strength aluminium alloy joints with button cracks on the mechanical strength. J Mater Sci Technol Res 2018;5:16–27. https://doi.org/10.15377/2410-4701.2018.05.4.

[14] Pan B, Sun H, Shang SL, Wen W, Banu M, Simmer JC, et al. Corrosion behavior in aluminum/galvanized steel resistance spot welds and self-piercing riveting joints in salt spray environment. J Manuf Process 2021;70:608–20. https://doi.org/10.1016/j.jmapro.2021.08.052.

[15] Ma Y, Lou M, Li Y, Lin Z. Effect of rivet and die on self-piercing rivetability of AA6061-T6 and mild steel CR4 of different gauges. J Mater Process Technol 2018;251:282–94. https://doi.org/10.1016/J.JMATPROTEC.2017.08.020.

[16] Xu Y. Effects of factors on physical attributes of self-piercing riveted joints. Sci Technol Weld Join 2006;11:666–71. https://doi.org/10.1179/174329306X131866.

[17] Li D, Han L, Shergold M, Thornton M, Williams G. Influence of rivet tip geometry on the joint quality and mechanical strengths of self-piercing riveted aluminium joints. Mater Sci Forum 2013;765:746–50. https://doi.org/10.4028/www.scientific.net/MSF.765.746.

[18] Wang B, Hao C, Zhang J, Zhang H. A new self-piercing riveting process and strength evaluation. J Manuf Sci Eng Trans ASME 2006;128:580–7. https://doi.org/10.1115/1.2137746.

[19] Han S-LL, Li Z-YY, Zeng Q-LL, Gao Y, Zeng Q-LL. Numerical Study on Die Design Parameters of Self-Pierce Riveting Process Based on Orthogonal Test. J Shanghai Jiaotong Univ 2014;19:308–12. https://doi.org/10.1007/s12204-014-1504-8.

[20] Jäckel M, Falk T, Landgrebe D. Concept for further development of self-pierce riveting by using cyber physical systems. Procedia CIRP 2016;44:293–7. https://doi.org/10.1016/j.procir.2016.02.073.

[21] Qu SG, Deng WJ. Finite element simulation of the self-piercing riveting process. ASME Int. Mech. Eng. Congr. Expo. Proc., vol. 4, 2008, p. 243–9. https://doi.org/10.1115/IMECE2008-67017.

[22] Mucha J. A study of quality parameters and behaviour of self-piercing riveted aluminium sheets with different

joining conditions. Stroj Vestnik/Journal Mech Eng 2011;57:323–33. https://doi.org/10.5545/sv-jme.2009.043.

[23] Li D, Chrysanthou A, Patel I, Williams G. Self-piercing riveting-a review. Int J Adv Manuf Technol 2017;92:1777–824. https://doi.org/10.1007/s00170-017-0156-x.

[24] Ang HQ. An Overview of Self-piercing Riveting Process with Focus on Joint Failures, Corrosion Issues and Optimisation Techniques. Chinese J Mech Eng (English Ed 2021;34:1–25. https://doi.org/10.1186/s10033-020-00526-3.

[25] Haque R, Beynon JH, Durandet Y. Characterisation of force–displacement curve in self-pierce riveting. Sci Technol Weld Join 2012;17:6:476–88. https://doi.org/10.1179/1362171812Y.0000000036.

[26] Haque R, Williams NS, Blacket SE, Durandet Y. A simple but effective model for characterizing SPR joints in steel sheet. J Mater Process Technol 2015;223:225–31. https://doi.org/10.1016/j.jmatprotec.2015.04.006.

[27] Li D. Influence of aluminium sheet surface modification on the self-piercing riveting process and the joint static lap shear strength. Int J Adv Manuf Technol 2017;93:2685–95. https://doi.org/10.1007/s00170-017-0710-6.

[28] Abe Y, Kato T, Mori K. Self-piercing riveting of high tensile strength steel and aluminium alloy sheets using conventional rivet and die. J Mater Process Technol 2009;209:3914–22. https://doi.org/10.1016/j.jmatprotec.2008.09.007.

[29] Mori K, Kato T, Abe Y, Ravshanbek Y. Plastic joining of ultra high strength steel and aluminium alloy sheets by self piercing rivet. CIRP Ann - Manuf Technol 2006;55:283–6. https://doi.org/10.1016/S0007-8506(07)60417-X.

[30] Hoang N-H, Hopperstad OS, Langseth M, Westermann I. Failure of aluminium self-piercing rivets: An experimental and numerical study. Mater Des 2013;49:323–35. https://doi.org/10.1016/J.MATDES.2013.01.034.

[31] He X, Xing B, Zeng K, Gu F, Ball A. Numerical and experimental investigations of self-piercing riveting. Int J Adv Manuf Technol 2013;69:715–21. https://doi.org/10.1007/s00170-013-5072-0.

[32] Han L, Thornton M, Shergold M. A comparison of the mechanical behaviour of self-piercing riveted and resistance spot welded aluminium sheets for the automotive industry. Mater Des 2010;31:1457–67. https://doi.org/10.1016/J.MATDES.2009.08.031.

[33] Haque R, Durandet Y. Investigation of self-pierce riveting (SPR) process data and specific joining events. J Manuf Process 2017;30:148–60. https://doi.org/10.1016/j.jmapro.2017.09.018.

[34] Zhao H, Han L, Liu Y, Liu X. Modelling and interaction analysis of the self-pierce riveting process using regression analysis and FEA. Int J Adv Manuf Technol 2021;113:159–76. https://doi.org/10.1007/s00170-020-06519-9.

[35] Carandente M, Dashwood RJ, Masters IG, Han L. Improvements in numerical simulation of the SPR process using a thermo-mechanical finite element analysis. J Mater Process Technol 2016;236:148–61. https://doi.org/10.1016/j.jmatprotec.2016.05.001.

[36] Hönsch F, Domitner J, Sommitsch C, Götzinger B, Kölz M. Numerical simulation and experimental validation of self-piercing riveting (SPR) of 6xxx aluminium alloys for automotive applications. J Phys Conf Ser 2018;1063:012081. https://doi.org/10.1088/1742-6596/1063/1/012081.

[37] Liu Y, Li H, Zhao H, Liu X. Effects of the die parameters on the self-piercing riveting process. Int J Adv Manuf Technol 2019;105:3353–68. https://doi.org/10.1007/s00170-019-04567-4.